DESIGN AND OPTIMIZATION OF COMPUTATIONALLY EXPENSIVE ENGINEERING SYSTEMS

BY

LAKSHMI GURURAJA RAO

THESIS

Submitted in partial fulfillment of the requirements
for the degree of Master of Science in Industrial Engineering
in the Graduate College of the
University of Illinois at Urbana-Champaign, 2015

Urbana, Illinois

Adviser:

Assistant Professor James T. Allison

Abstract

Engineering systems form the basis on which our day-to-day lives depend on. In many cases, designers are interested in identifying an optimal design of an engineering system. However, very often, the process of engineering design optimization is complex and involves time-expensive simulations or the need to satisfy not just one, but multiple objectives. This thesis aims to explore the area of efficient optimization algorithms applied to engineering system design. In particular, the engineering systems discussed here involve the use of rheologically complex materials. Engineers face many modeling challenges while trying to design systems with rheological materials, pertaining to mathematical modeling and optimization. However, the use of more flexible design methods in conjunction with rheologically complex materials enhances design freedom and diffuses design fixation. The first part of the thesis discusses the characteristics of such materials and introduces their usage in engineering design. A second kind of complex systems include the ones characterized by multiple objectives and time-expensive simulations. Design optimization is a cumbersome process in such a case. Using an approximation or a surrogate model of this kind of system helps to mitigate computational costs. The use of an adaptive surrogate modeling alogrithm (along with optimization) is demonstrated on such systems, that involve the use of complex fluids. The unifying theme of the thesis is the application of efficient optimization algorithms to computationally expensive material design problems. In this thesis, we introduce the use of direct optimal control to identify optimal material function targets. The thesis also details a novel adaptive surrogate modeling algorithm that was developed to solve multi-objective optimization problems. Both these ideas are demonstrated with the help of case studies and analytical examples.

To my parents, for their unconditional love and support.

Acknowledgments

First and foremost, I would like to extend my gratitude to Prof. James T. Allison, for having given me this opportunity to work with him and for moulding me into the researcher I am today. His unwavering patience, insightful advice and constant support have been valuable to me during my graduate school experience. I also had the pleasure of working with Prof. Randy H. Ewoldt, at the Mechanical Science and Engineering department, UIUC. Both the research projects that are discussed in this thesis were the result of a collaborative effort with Prof. Ewoldt's research group. What seemed to me like a new and (hence) intimidating area of research initially, was greatly simplified thanks to the numerous interesting discussions with Prof. Ewoldt.

I wish to thank my fellow graduate students at the Engineering Systems Design Lab (ESDL) - Anand, Dan, Tinghao, Jeff, Ashish, Jason, Danny and Adam. I have enjoyed the conversations at 406 TB, that were not always (almost always not) about research. I have always received help and support and a wondrous bout of good humor when I have needed it, and I am extremely grateful for that. I am more than grateful to the ISE department for supporting me through Teaching Assistantships and I deeply appreciate the kindness and help I received from Holly Kizer and the other adminstrative staff, right from the day I started my Master's program.

I was fortunate to work with Rebecca Corman and Jonathon Schuh from Prof. Ewoldt's research group. They made the many hours spent at MEL more enjoyable and hence, more fruitful. I would like to thank Yong Hoon Lee for his tireless work in the recent past, with regards to both my research projects.

My acknowledgement would be incomplete without mentioning Neal Davis, from the Computational Science and Engineering department for our many conversations about Python, Julia and theories of science and research. I am

thankful for the TA experience he provided me with, and feel fortunate for having met an inspirational person such as him, during my graduate school life. One of the earliest inspirations came from Prof. Andreas Kloeckner at the Computer Science department, UIUC, when I took his course on Numerical Analysis in Spring 2014. I greatly benefited from the course, his encouraging words and honest professional advice.

Last but definitely not the least, I would like to thank my family of friends here at Champaign - my roommate, Aparna, who, aside from being my go-to graphics guide, has been a tremendous sense of support; Sundar, Sabareesh and Yashwant, for being a part of some of my best times here and a whole bunch of others who can make my acknowledgement run into pages. I am extremely thankful to Preethi and Shridhar (at the Ohio State University) for having faith in my abilities, even at times when I did not believe in them, myself. I was lucky to live close to my immediate family at Purdue. I wish to thank my uncle, for being my role model since the time I was young and encouraging me to always aim high; my aunt, for being a wonderful host and my six-year-old cousin, Mukund, for showing me the best kind of affection. Finally, I would like to thank my parents and my grandparents back home, who have always been a positive influence and have given me the utmost freedom and carved out opportunities for me, at every stage of my life.

TABLE OF CONTENTS

List of Tables viii

List of Figures ix

Nomenclature xi

CHAPTER 1 Introduction 1

CHAPTER 2 Rheological materials 4
2.1 Engineering Design with soft materials 4
2.2 Viscoelastic materials 5

CHAPTER 3 Design Optimization via material function targets 14
3.1 Relaxation Modulus as the target function 14
3.2 Parameterizations of $K(t)$ 18
3.3 Generalized viscoelastic model 21
3.4 Integro-Differential Equations (IDEs) 23
3.5 Optimal Control methods 25

CHAPTER 4 Numerical Studies on a vibration isolator - Part 1 31
4.1 Case study 31
4.2 Results 34

CHAPTER 5 Numerical Studies on a vibration isolator - Part 2 43
5.1 Formulation of the optimal control problem 43
5.2 A single shooting approach 46
5.3 Direct Transcription 49
5.4 Results 50
5.5 Conclusions 51

CHAPTER 6 Adaptive Surrogate Modeling based Multi-Objective Optimization 56
6.1 Adaptive SM Methodology 57
6.2 ASM-MOO Algorithm Framework 59

CHAPTER 7 Numerical Studies and Results using Adaptive Surrogate Modeling 69
7.1 Analytical Example 69
7.2 Design for Efficient Fluid Power 71
7.3 Conclusions and Future Work 76

CHAPTER 8 Conclusion 77

APPENDIX A High Frequency scaling of displacement amplitude 78
A.1 Initial Case (Spring only) 78
A.2 Spring + Linear Dashpot 79
A.3 Spring + Generalized Viscoelastic Element 79

REFERENCES 85

List of Tables

3.1 Relaxation kernel $K(t)$ for 1-D systems 15

4.1 Optimization results for the vibration isolator case study based on existing viscoelastic models 36
4.2 Optimization results from the extension of vibration isolator case study with existing viscoelastic models and over a range of frequencies 40

5.1 Optimal objective function values from Single Shooting and Direct Transcription 51

7.1 Analytical Problem - Results 71
7.2 Measured Geometric Parameters. 72
7.3 Case Study - Results 75

List of Figures

2.1 Product Design Process 5
2.2 Creep and Stress Relaxation plots 7
2.3 Dynamic Loading and Hysteresis 8
2.4 Maxwell model for a viscoelastic material. 11
2.5 Kelvin-Voigt model for a viscoelastic material. 12

3.1 Parameterizations of $K(t)$ 20
3.2 A discrete topology can be generalized by the introduction of a viscoelastic element. 22
3.3 Convolution example 29
3.4 Convolution of $f(t)$ and $g(t)$ 30

4.1 Design of optimal viscoelastic vibration isolation for a 1-dimensional spring-mass system 31
4.2 Design involving a generalized viscoelastic element with relaxation kernel $K(t)$ 35
4.3 Optimized performance and design 38
4.4 Case Study extension 39
4.5 Results of the case study extension to a range of natural frequencies 41

5.1 Direct Optimal Control applied to the case study 45
5.2 Convolution sum validation 46
5.3 Unstable Dynamics 48
5.4 Optimal State trajectories of Single Shooting and Direct Transcription implementations 52
5.5 Optimal $K(t)$ trajectories of Single Shooting and Direct Transcription implementations 53

6.1 Strategies for SM-based design optimization 58
6.2 ASM-MOO algorithm 60
6.3 Octree-based sampling algorithm to update the sampling domain 67
6.4 Conceptual illustration of validation point and sample point generation 68

7.1 Analytical Problem - Pareto set 70
7.2 Analytical Problem - Pareto design values 70
7.3 Experimental setup. Design variables are defined in Eqn. (7.2). 72
7.4 Case Study - Pareto set in design space 74
7.5 Case Study - Pareto set 75

Nomenclature

$\boldsymbol{\phi}(\cdot)$	Boundary constraints in optimal control
$\boldsymbol{\psi}$	Gram matrix of the Radial Basis Functions
$\boldsymbol{\xi}$	Dynamic system state variable vector
$\boldsymbol{\Xi}(\cdot)$	Discretized states in direct transcription
$\boldsymbol{\zeta}(\cdot)$	Defect constraints in direct transcription
$\epsilon(t)$	Strain
η, λ	Maxwell Parameters
η_a	Apparent viscosity of fluid power problem
$\hat{\mathbf{f}}(\cdot)$	Approximate Objective function of MOO
$\hat{\mathbf{g}}(\cdot)$	Approximate Inequality constraint of MOO
$\hat{\mathbf{h}}(\cdot)$	Approximate Equality constraint of MOO
$\mathbf{C}(\cdot)$	Path constraints in optimal control
$\mathbf{f_d}$	State derivative function optimal control
$\mathbf{f}(\cdot)$	Objective function of MOO
$\mathbf{g}(\cdot)$	Inequality constraint of MOO
$\mathbf{h}(\cdot)$	Equality constraint of MOO
$\mathbf{I}$	Convolution sum
$\mathbf{u}$	Control input in optimal control

$\mathbf{w}$ Weights of the Radial Basis Functions

$\mathbf{x}_*$ Optimal design variable

$\mathbf{x}_{LB}, \mathbf{x}_{UB}$ Lower and upper bounds of design variables of MOO

$\mathcal{L}(\cdot)$ Lagrangian cost function in optimal control

$\mathcal{M}(\cdot)$ Meyer cost function in optimal control

$\sigma(t)$ Stress

$\tilde{\omega^*}$ Natural frequency

$\tilde{D}_s$ The sampling domain, from which sampling points are taken

$\tilde{D}_u$ Updated sampling domain

D Texture depth of fluid power problem

D_m The modeling domain that forms the basis for the surrogate model construction

D_s Feasible Sampling Domain

D_u Updated feasible sampling domain

D_v Validation domain

F Feasible domain

h Gap height of fluid power problem

h_k kth Time step size

k Spring constant

$K(t)$ Relaxation Modulus

$K''(\omega)$ Dynamic Loss Modulus

$K'(\omega)$ Dynamic Storage Modulus

L Plate length of fluid power problem

m Mass

n_t Number of time steps

S_k, n Critical Gel Parameters

T Training Data Set

U Velocity of plate of fluid power problem

W Texture width of fluid power problem

$x, \dot{x}, \ddot{x}$ Position, Velocity, Acceleration

CHAPTER 1

Introduction

Engineering systems form the basis on which our day-to-day lives depend on. Starting from the thermostat that keeps you comfortable in any kind of temperature to the electrical energy of the satellite orbiting in space, which helps you watch television at home, engineering systems have found vast and diverse applications in the real world. The design of such systems is a challenging task, which involves the understanding of the physics behind the system as well as the practical viability of the design methodology.

The primary step in engineering design involves modeling the system. Physical models are constructed, where resources and labor are available. Computer-based models of engineering systems and simulation of these models started around the time of World War II [1]. Today, most engineering systems are modeled with the help of virtual experiments. This serves as a cost-effective methodology for both designing, testing and making changes to the existing model and is advantageous in cases where physical modeling is not feasible. However, there exist many complex engineering systems, whose virtual modeling is computationally demanding. Despite advances in computing power in the recent past, computationally intensive analysis methods such as Finite Element Analysis (FEA) and Computational Fluid Dynamics (CFD) require efficient numerical treatment [2]

In most design problems, engineers are interested in identifying an optimal design of the system being modeled. The next step in the design process is optimization of the engineering system. Computerized models can be optimized by the use of various optimization algorithms that have been developed [3]. However, when the simulation of the engineering system is time-expensive, optimization of the system consumes a lot of computing time. For example, forecasting weather is an expensive computer simulation based on various atmospheric factors. If we wished to maximize the amount of solar energy conserved on a given day, we would need to run the simulation multiple

times to understand which time of the day recorded the highest range of temperature, each simulation requiring significant running time. An efficient optimization technique is essential in order to minimize running time and computational complexity.

In this thesis, two such optimization routines are presented, which are applied to engineering systems characterized by time-intensive simulations: (1) Surrogate modeling, which involves building a data-model of the physical system and using the data model for the purposes of optimization. (2) Direct Optimal Control, which is a class of optimal control routines applied to a dynamic system in order to minimize a cost function associated with it.

The application of these two routines is in the domain of engineering material design. Material design is a field with vast applications. Materials are classified as hard or soft based on their inherent material compliance [4]. In naïve terms, soft materials are more flexible and exhibit deformation when subject to a force, as opposed to brittle materials. While designing materials for engineering systems, engineers have primarily used hard materials. The complexity of soft materials arises from their unconventional microstructures. The resulting complexity is carried forward in the modeling of such materials. Utilizing such materials in engineering design requires specialized modeling and optimization methods. While complex in nature and modeling, the different dynamics of soft materials result in fascinating engineering applications. The need to use these materials, despite their complexity, thus stems from the desire to explore the design space, enhance design freedom and motivate system-level design.

The unifying theme of the thesis is to address the optimization of engineering problems that are time-consuming in their simulation. The thesis is structured in the following manner. Chapter 2 sets the backdrop of the application, by further explaining complex materials and the challenges encountered in their mathematical modeling. The chapter also discusses the need to develop efficient numerical methods to model complex materials and gives a gentle introduction to different methods that are used for the efficient handling of expensive simulations. It is followed by Chapter 3, which goes into numerical details and formulation of an efficient optimization technique utilizing optimal control. This is presented with the help of a case study involving a vibration attenuation problem in Chapter 4 and 5. The focus is then shifted to the use of surrogate modeling in Chapter 6. The application

of surrogate modeling to alleviate the cost of time-expensive problems is discussed with a detailed case study in Chapter 7. The results, discussions and future work are enumerated in Chapter 8.

CHAPTER 2

Rheological materials

Rheology pertains to the study of flow of matter, primarily in a liquid state. It applies to *soft solids* that respond with a plastic flow rather than elastic deformation, when subject to an external force [5] . It includes the study of materials that have a complex microstructure such as muds, sledges, foods and additives like ketchup, mayonnaise and other such soft materials.

Soft matter includes elastomers, polymers, colloids, gels, emulsions, surfactants, suspensions, granular materials, and liquid crystals. These materials are also referred to as complex fluids [6].

2.1 Engineering Design with soft materials

While using materials in engineering design, designers typically use hard materials or simple fluids. The advantages of using soft, rheologically complex materials are demonstrated by many biological systems [7–9]. Soft, rheologically-complex materials can show dramatic transitions from elastic (solid-like) to viscous (fluid-like) behavior as a function of various parameters, including timescales (viscoelasticity), amplitude (shear-thinning, extensional thickening), or external fields. These inherent characteristics result in novel performance which has engineering applications [4]. Soft materials have not been a component of conventional design as they are characterized by function-valued quantities that depend on frequency (linear viscoelasticity), input amplitude (as in the case of non-linear material responses) or more generally, both. The options for direct mathematical-modeling with material properties (which we consider design-driven or design-friendly modeling) is not fully clear. In the case where soft materials are used for system design, the design is usually material-specific. While this is a useful tool in many design problems, it limits design freedom. For example, viscoelastic

functionality may come from polymers, colloids, and many other forms of structured soft materials. An early stage material-agnostic approach places fewer structural restrictions on the design space, and may help avoid design fixation [10, 11]. Previous work identified need for system-level material design [12]. The focus of this kind of system-level design approach is not the material itself, but its functionality. Figure 2.1 illustrates the strategy of using a system-level approach in the design of rheologically complex materials. We envision a multi-level system design process that is material-agnostic at early stages but material-specific at later stages (as shown in Fig. 2.1). This multi-level hierarchical problem will connect functional system performance down to rheological properties, and finally down to the material formulation. This thesis aims to explore the use of a specific class of soft materials, known

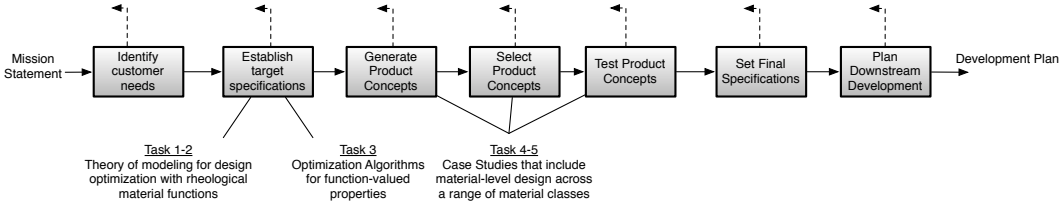

Figure 2.1: Different elements of the concept development aspect of the product design process that can be applied to rheologically-complex materials (design process adapted from Ulrich and Eppinger [13])

as viscoelastic materials in engineering design systems. While this chapter focuses on understanding and modeling viscoelastic materials and its associated difficulties, Chapter 3 will detail a modeling and optimization approach toward using viscoelastic materials in engineering design.

2.2 Viscoelastic materials

Viscoelastic materials (as the name suggests) display both viscous and elastic characteristics while undergoing deformation. Viscous materials, resist a deformation (induced by a shear stress) by deforming linearly with time. Elastic materials quickly return to their original form, when stretched. Viscoelastic materials inherit both these behaviors and demonstrate time-dependent strain. They respond differently depending on how fast the stress is applied.

For instance, if a silly putty (which is an example of a viscoelastic material) is stretched slowly, the material elongates slowly and demonstrates a viscous fluid-like behavior. On the other hand, if it is stretched too quickly, it breaks without any displacement and behaves more like a solid. Thus, the strain is dependent on the rate of the stress applied.

Viscoelasticity arises from the microstructure of the material. In the characterization of viscoelastic materials, typically three important tensile tests are performed, namely: (1) Creep Deformation (2) Stress Relaxation, and (3) Dynamic Loading.

2.2.1 Creep

In the creep tests, the viscoelastic material is subjected to a steady uniaxial stress σ_0 and the resulting time-dependent strain $\epsilon(t)$ is studied. [14]

$$\epsilon(t) = \delta(t)/L_0 \tag{2.1}$$

If doubling the constant stress σ_0 doubles the strain, then the material is said to be *linear* i.e. displays a linear stress-strain relationship. The creep compliance $J(t)$ is then computed as the ratio between the strain and stress.

$$J(t) = \frac{\epsilon(t)}{\sigma_0} \tag{2.2}$$

2.2.2 Stress relaxation

Another common test performed on viscoelastic materials is studying time-dependent stress, $\sigma(t)$ resulting from a constant strain, ϵ_0. The relaxation modulus $K(t)$ is then computed as:

$$K(t) = \frac{\sigma(t)}{\epsilon_0} \tag{2.3}$$

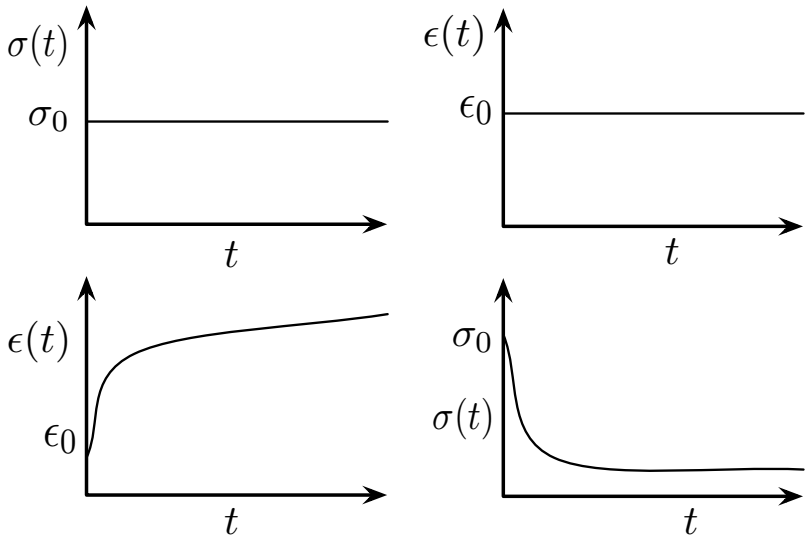

(a) Creep test on a viscoelastic material

(b) Stress Relaxation test on a viscoelastic material

Figure 2.2: Creep and Stress Relaxation plots

2.2.3 Dynamic Loading

Creep deformation and stress relaxation are helpful in understanding long term phenomena associated with viscoelastic materials. However, to understand the short-term response behavior, using a dynamic loading test proves to be useful. When a viscoelastic material is subjected to a sinusoidally varying stress, a steady state will eventually be reached in which the resulting strain is also sinusoidal, having the same angular frequency but retarded in phase by an angle δ.

Let us consider the following representations for ϵ and σ:

$$\epsilon = \epsilon_0 \cos \omega t \tag{2.4}$$

$$\sigma = \sigma_0 \cos(\omega t + \delta) \tag{2.5}$$

Writing the stress as a sum of two components, one in-phase with the strain and one out-of-phase give us:

$$\sigma^* = \sigma_0' \cos \omega t + i\sigma_0'' \sin \omega t \tag{2.6}$$

where,

$$\sigma_0' = \sigma_0 \cos\delta$$
$$\sigma_0'' = \sigma_0 \sin\delta$$

The two representations are used to define two dynamic moduli, both being ratios of stress to strain but differing in molecular interpretations.

$$\text{Storage Modulus} \qquad K' = \frac{\sigma_0'}{\epsilon_0} \tag{2.7}$$

$$\text{Loss Modulus} \qquad K'' = \frac{\sigma_0''}{\epsilon_0} \tag{2.8}$$

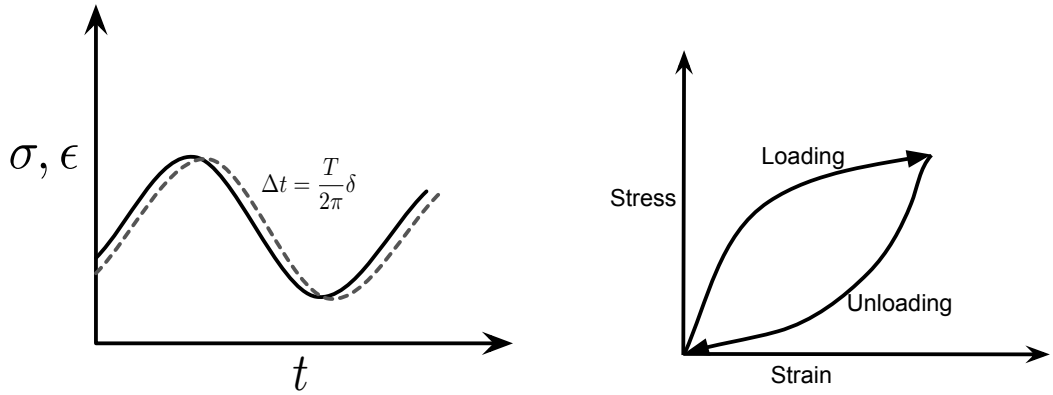

(a) Dynamic Loading Test - the strain lags the stress by a time period of $\frac{T}{2\pi}\delta$

(b) Hysteresis in viscoelastic materials. The energy absorbed is given by the area of the graph.

Figure 2.3: Dynamic Loading and Hysteresis plots for a viscoelastic material

2.2.4 Hysteresis in viscoelastic materials

Consider the mechanical work done per loading cycle (with a frequency of ω) for the dynamic load described above:

$$W = \oint \sigma d\epsilon = \oint \sigma \frac{d\epsilon}{dt} dt \tag{2.9}$$

With a time period $T = 2\pi/\omega$, and using the expressions for ϵ from Eqn. 2.5 and σ from Eqn. 2.6, W can be evaluated as:

$$W = \int_0^{2\pi/\omega} (\sigma_0' \cos\omega t)(-\epsilon_0 \omega \sin\omega t)dt + \int_0^{2\pi/\omega} (\sigma_0'' \sin\omega t)(-\epsilon_0 \omega \sin\omega t)dt \tag{2.10}$$

Solving the integrals gives us:

$$W = 0 - \pi\sigma_0''\epsilon_0 \tag{2.11}$$

Thus, some energy is dissipated during the loading cycle. This phenomenon is an example of hysteresis. Hysteresis in a system arises when the output response of the system depends not only on the current but also past inputs, which in this case is due to the loss of some energy. The stress-strain relationship during the loading cycle is show in Fig. 2.3(b).

Apart from viscoelastic systems, there are other engineering and biological systems that exhibit other kinds of hysteresis such as electromagnets. Hysteresis need not necessarily relate to the same underlying physical variable. Viscoelastic materials undergo hysteresis based on the energy dissipated during dynamic loading. In aircraft wing aerodynamics, hysteresis can be observed when the angle of attack where the flow on top of the wing reattaches is generally lower than the angle of attack where the flow separates [15]. Physical adsorption is another example that exhibits the unusual property, where it is possible to scan within the hysteresis loop by reversing the direction of adsorption. [16].

2.2.5 Linear Viscoelasticity

A linear viscoelastic material is one which has a linear relationship between its strain history and stress.

$$\sigma(t) = \int_{-\infty}^{t} K(t - t')\dot{\epsilon}(t')dt' \tag{2.12}$$

Here, $K(t)$ is the **relaxation modulus** of the material, which is the function-valued property that we will attempt to design. In other words this thesis aims to identify an optimal shear modulus function for a material in order to satisfy certain objectives (which will be explained with the help of a case

study in the following chapters). Though linear viscoelasticity is an idealized representation of physical materials in the real world, it forms a good basis to understand and study such complex rheological materials.

2.2.6 Mathematical models of viscoelastic materials

To ensure an optimal design of viscoelastic materials based on the functionality it aims to serve, a mathematical model of the material is required. In this section, a systematic approach is established for mathematically modeling linear viscoelastic materials, for understanding the implications of generalized viscoelastic design and for addressing the challenges that its optimization entails.

A common mechanical paradigm used in the study of viscoelastic models is a combination of springs and dashpots. While a spring-dashpot model does not directly represent the microstructure of viscoelastic materials, it helps us visualize molecular motions. The spring (with a spring constant k) accounts for the elastic component of the material and obeys Hookean spring laws.

$$\sigma = k\epsilon \tag{2.13}$$

The spring constant k is analogous to the Young's modulus E and σ and ϵ are similar to the spring force and displacement respectively.

The viscous component is represented by a Newtonian dashpot (with a viscosity c).

$$\sigma = c\dot{\epsilon} \tag{2.14}$$

The ratio between c and k is often used as a measure of viscoelastic response time.

$$K_0 = \frac{c}{k} \tag{2.15}$$

Based on the arrangement and number of springs and dashpots, there are a number of possible representations. We discuss the most basic viscoelastic models which make use of one spring and dashpot, namely (1) Maxwell model (2) Kelvin-Voigt Model.

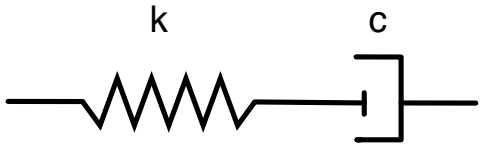

Figure 2.4: Maxwell model for a viscoelastic material.

Maxwell Model

The Maxwell model consists of a spring and dashpot in series (as shown in Fig. 2.4). Given a stress σ acting on the Maxwell element, the stress across the spring and dashpot are the same, while the strain is split between the two elements. The equilibrium equation is written as:

$$\sigma = \sigma_s = \sigma_d \tag{2.16}$$

$$\epsilon = \epsilon_s + \epsilon_d \tag{2.17}$$

$$\tag{2.18}$$

The subscripts s and d refer to the spring and dashpot respectively. To arrive at a constitutive equation:

$$\dot{\epsilon} = \dot{\epsilon_s} + \dot{\epsilon_d} = \frac{\dot{\sigma}}{k} + \frac{\sigma}{c} \tag{2.19}$$

Using Eqn.(2.15) we can rewrite the above equation as:

$$k\dot{\epsilon} = \dot{\sigma} + \frac{\sigma}{K_0} \tag{2.20}$$

Stress Relaxation: Maxwell Model

In the stress relaxation test, the strain is maintained at a constant value. Thus, $\dot{\epsilon} = 0$. Eqn. (2.20) now becomes:

$$\frac{d\sigma}{dt} = -\frac{\sigma}{K_0} \tag{2.21}$$

The above differential equation can be solved simply to find the expression for strain.

$$\sigma(t) = \sigma_0 e^{-t/K_0} \tag{2.22}$$

Kelvin-Voigt Model

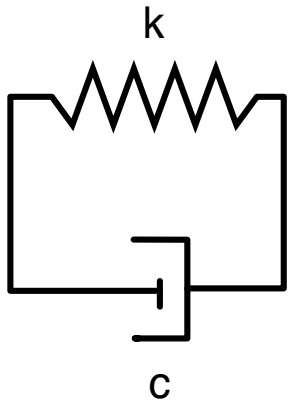

Figure 2.5: Kelvin-Voigt model for a viscoelastic material.

Another basic viscoelastic model is a parallel arrangement of the spring and the dashpot. In this model, an applied load is supported by the spring and the dashpot. The equilibrium equations can be written as:

$$\sigma = \sigma_s + \sigma_d \tag{2.23}$$

$$\epsilon = \epsilon_s = \epsilon_d \tag{2.24}$$

The subscripts s and d refer to the spring and dashpot respectively. Using Eqn. (2.15), the stress can be written as:

$$\sigma = k\epsilon_s + c\dot{\epsilon_d} \tag{2.25}$$

Creep: Kelvin Voigt Model

A creep test uses a constant stress and studies the strain rate. If a load σ_0 is applied suddenly to the Kelvin-Voigt model, the spring will want to stretch, but is held back by the dash-pot, which cannot react immediately. The resulting differential equation, when solved leads to the following expression for strain.

$$\epsilon(t) = \frac{\sigma_0}{k}(1 - e^{-\frac{t}{K_0}}) \tag{2.26}$$

2.2.7 Motivation to study viscoelastic materials

Having understood viscoelastic behavior, it is important to understand why they should be studied. They are widely prevalent in biological, engineering, and other physical systems. The disks in the human spine are viscoelastic and undergo creep due to body weight. They grow shorter with time. Lying down reduces the stress on the disks and thereby helps them recover. Most people are hence taller in the mornings than in the evening. Astronauts gained up to 5 cm under zero gravity conditions [14].

Creep is also the reason behind the sagging of wooden structures over time. Polymer foam cushions used on couches and chairs also undergo creep on prolonged application of pressure and conform to the shape of the person sitting on them. Such is the case with metal turbine blades in jet engines, which reach very high temperatures and need to withstand very high tensile stresses. Conventional metals can creep significantly at high temperatures. A newly born baby's head is viscoelastic and its ability to creep and recover helps in the birthing process. If the baby sleeps in a particular position for long, its head can become misshapen due to creep deformation. Bolts and screws used in machine components, when subjected to high temperatures, undergo stress relaxation and loosen over time [14].

Understanding the behavior of viscoelastic materials is the first step to utilizing them in engineering design. Leveraging viscoelastic response to design better engineering systems is the goal of this research work. Viscoelastic materials are excellent impact absorbers. Viscoelastic materials are used in car bumpers, on computer drives to protect from mechanical shock, in helmets (the foam padding inside), in wrestling mats, etc. They are also used in shoe insoles to reduce impact transmitted to a person's foot. Acoustic blankets made of viscoelastic materials is used to attenuate the noise from helicopters. Dampers made of such materials are also used to protect high rise buildings from the impact of turbulent winds.

Chapters 3, 4 and 5 will detail the use of viscoelastic materials in engineering design and the optimization techniques that can be utilized in identifying optimal material functions, thus enabling material-agnostic design and enhancing design freedom.

CHAPTER 3

Design Optimization via material function targets

The first step to understanding material design optimization is to identify the material property that we wish to control. In other words, our aim is to design a viscoelastic material property function which will achieve certain design objectives. For instance, in the design of a shock absorber with viscoelastic materials, if we choose our material function as the relaxation modulus $K(t)$, we would then formulate our optimization problem to identify an optimal target function $K(t)$ that would minimize the shock (physically quantified as acceleration).

As a preliminary step of implementing functionality-driven viscoelastic design, we utilize existing viscoelastic models and parameterizations of $K(t)$. While this serves as a good exercise to understanding the system and its optimal target function, we identify the need to incorporate generalized viscoelastic design, that does not involve any a priori assumptions on $K(t)$. The use of optimal control methods in the identification of optimal material target functions is also discussed in this chapter.

3.1 Relaxation Modulus as the target function

As defined in Chapter 2, the relaxation modulus of a viscoelastic material is the ratio between the stress and the constant strain in a stress relaxation test.

$$K(t) = \frac{\sigma(t)}{\epsilon_0} \tag{3.1}$$

Here we consider one-dimensional deformation, and thus are able to represent the force through the viscoelastic connection with a single scalar equa-

Table 3.1: Relaxation kernel, $K(t)$, for the generalized viscoelastic component as shown in Fig. 3.2. For 1-D systems, extrinsic component measures can be transformed to intrinsic material measures by a linear mapping depending on component geometry. The relaxation kernel is the design parameter as the dynamic storage and loss moduli are related through the Kramers-Kroenig relations, and thus not fully independent (Eqs.3.9 and 3.9).

	Force connection $K \doteq [F/L]$	**Material (extension)** $E \doteq [F/L^2]$	**Material (shear)** $G \doteq [F/L^2]$
Proportionality	Force-Displacement	Stress-Strain	Stress-Strain
Relaxation Kernel	$K(t)$	$E(t)$	$G(t)$
Dynamic Storage	$K'(\omega)$	$E'(\omega)$	$G'(\omega)$
Dynamic Loss	$K''(\omega)$	$E''(\omega)$	$G''(\omega)$

tion:

$$F_{ve}(t) = \int_{-\infty}^{t} K(t-t')\dot{X}(t')dt' \tag{3.2}$$

where F_{ve} is the force due to a viscoelastic element, $\dot{X}$ is the deformation velocity experienced by the element (dimensions $\dot{X} \doteq [\mathrm{LT}^{-1}]$) and the force relaxation kernel $K(t-t') \doteq [\mathrm{FL}^{-1}]$. With a change of variable $s = t - t'$ this convolution integral becomes:

$$F_{ve}(t) = \int_{0}^{\infty} K(s)\dot{X}(t-s)ds. \tag{3.3}$$

If the viscoelastic properties arise from a continuum of material, we can make an analogy from extensive properties (force, velocity, stiffness) to intensive material properties (stress, strain, modulus), and therefore complex strain fields within the isotropic linear viscoelastic regime (see Table 3.1). The relaxation kernel $K(t)$ that relates the extrinsic measures of force and displacement is transformed to its analogous material measures $E(t)$ (in ex-

tension) or $G(t)$ (in shear) which relate the intrinsic measures of stress and strain through a linear mapping of area divided by length (dimensions $[L]$) based on geometry. A simple example of the relationship between the extrinsic and intrinsic measures is shown in one-dimensional tension where the intrinsic measures stress and strain are related through material connection function E (Table 3.1) by $\sigma = E\epsilon$. Converting these measures to their extrinsic equivalents requires the geometrical relations $\sigma = F/A$ and $\epsilon = x/L$. Combining these relations leads to the extrinsic form of Hooke's law, $F = (EA/L)\, x$. Where the extrinsic force connection kernel K can be written as $K = EA/L \doteq [F/L]$.

In the isotropic, incompressible, linear viscoelastic regime, the descriptive kernel function, the stress relaxation modulus, is the measured stress response to a step change in strain, which can be used generally in Boltzmann superpostion [4, 17]. The modulus is equivalent to a predictive constitutive model parameter, and can be used to compute any three-dimensional deformation history. By analogy to Eqn. (3.2), the 3-D expression for the Boltzmann superposition integral uses the relaxation modulus $G(t)$, in tensorial form:

$$\underline{\underline{\sigma}}(t) = \int_{-\infty}^{t} G(t-t')\dot{\underline{\underline{\gamma}}}(t')dt', \tag{3.4}$$

where $\underline{\underline{\sigma}}(t)$ is the Cauchy stress tensor, and the strain-rate tensor is:

$$\dot{\underline{\underline{\gamma}}} = \underline{\nabla}\ \underline{v} + (\underline{\nabla}\ \underline{v})^{\mathrm{T}}, \tag{3.5}$$

where $\underline{v}$ is the velocity field and we define the velocity gradient as $(\underline{\nabla}\ \underline{v})_{ij} = \partial v_j/\partial x_i$. Equation (3.4) is limited to small deformation in the linear viscoelastic regime for incompressible materials, but applies for any class of linear viscoelastic material (elastomer, composite, polymeric liquid, colloid, gel, etc.) falling within the framework of a continuum description.

The relaxation kernel $K(t)$ is treated here as an independent design variable. Alternative viscoelastic material functions, such as the creep compliance $J(t)$, can also be used to define a relation similar to Eqn. (3.4) with the displacement field as the output of the integral. This may be mathematically convenient for load-control inputs. However, in the linear viscoelastic limit, all of the the material functions are interrelated [18], and therefore only one single-valued function can be specified in the design.

Linear viscoelastic materials are commonly described in the frequency-domain, such as the dynamic storage and loss moduli are shown in Table 3.1. For a viscoelastic fluid (with stress relaxing to zero at infinite time) the dynamic storage and loss moduli are directly related to $K(t)$ as

$$K'(\omega) = \omega \int_0^\infty K(s) \sin(\omega s) ds \tag{3.6}$$

$$K''(\omega) = \omega \int_0^\infty K(s) \cos(\omega s) ds. \tag{3.7}$$

Additionally, the dynamic storage and loss moduli are combined to create a complex modulus of the form $K^* = K' + iK''$ where i is the imaginary unit.

Since each function is related to $K(t)$, the two functions are clearly not independent. As shown in Table 3.1, this holds true in the analogous material measures in extension ($E(t)$, $E'(\omega)$, $E''(\omega)$) and shear ($G(t)$, $G'(\omega)$, $G''(\omega)$). The interrelations are given by the Kramers-Kronig relations, shown here in terms of the dynamic moduli [17]

$$G'(\omega) - G'(\infty) = \frac{2}{\pi} \int_0^\infty \frac{x G''(x)}{\omega^2 - x^2} dx \tag{3.8}$$

$$G''(\omega) = \frac{2\omega}{\pi} \int_0^\infty \frac{G'(x)}{x^2 - \omega^2} dx \tag{3.9}$$

where we define:

$$G'(\infty) = \lim_{\omega \to \infty} G'(\omega) \tag{3.10}$$

Any in-phase and out-of-phase dynamic material functions must also satisfy these relations. With simple shear properties, this includes moduli G' and G'', viscosities η' and η'', compliances J' and J'', and fluidities ϕ' and ϕ'' [17,19]. The Kramers-Kronig relations also restrict the independent specification of frequency-dependent magnitude and phase angle.

The independent function $K(t)$ (or equivalently $G(t)$ or $E(t)$) is therefore treated as the function-valued design variable for linear viscoelasticity.

3.2 Parameterizations of $K(t)$

In general, the relaxation kernel, $K(t)$, can be treated as a function of arbitrary structure. Passive materials or systems impose the restriction that the function be monotonically decreasing [20, 21], however, this restriction on complexity could be lifted through the use of actively controlled systems. Complete freedom in the shape of the relaxation kernel presents difficulties for numerical optimization. For this initial exploration of $K(t)$ optimization, we consider several parameterizations of $K(t)$ with a finite number of design parameters as shown in Fig. 3.4: parameterization as a dashpot, a single and multi-mode Maxwell, and power law relaxation (analogous to a critical gel material) [22, 23].

For a standard, linear dashpot, the form of the relaxation kernel can be represented as:

$$K(t) = c \cdot \delta(t) \tag{3.11}$$

where $c \doteq [F/(L/T)]$ The dynamic coefficients for a linear dashpot are given by

$$K'(\omega) = 0 \tag{3.12}$$

$$K''(\omega) = c \cdot \omega \tag{3.13}$$

By analogy, a Newtonian fluid has $G(t) = \eta_0 \delta(t)$, $G' = 0$, and $G'' = \eta_0 \omega$. A Maxwell element is a linear spring and dashpot connected in series. It is the simplest model of a viscoelastic fluid. The model can be generalized to a multi-mode Maxwell model that includes M Maxwell elements connected in parallel. The relaxation kernel, also known as a Prony series, is defined by:

$$K(t) = \sum_{m=1}^{M} K_m e^{-t/\lambda_m}. \tag{3.14}$$

where K_m are the Maxwell spring constants ($K_m \doteq [F/L]$), and λ_m are the relaxation times ($\lambda_m \doteq [T]$). The Maxwell dashpot coefficient is $\eta_m = K_m \lambda_m$. Here we will consider the cases of $M = 1$ and $M = 3$ in order to limit the number of parameters ($2M$ parameters for an M-mode Maxwell model). For

this form, the dynamic coefficients of a force component connection are

$$K'(\omega) = \sum_{m=1}^{M} K_m \frac{(\lambda_m \omega)^2}{1 + (\lambda_m \omega)^2} \tag{3.15}$$

$$K''(\omega) = \sum_{m=1}^{M} K_m \frac{\lambda_m \omega}{1 + (\lambda_m \omega)^2}. \tag{3.16}$$

These are analogous to intrinsic material properties $G'(\omega)$, $G''(\omega)$ [see Table 3.1]. To achieve some functional forms of $K(t)$ such as power law behavior, a Maxwell model would require a large number of parameters. In order to include this broader design space, but with a small number of parameters, we will consider the critical gel power law model. Power-law rheology is an important signature, seen in materials near a gel point [23,24], food systems such as egg yolk [25], and active biological materials such as cells [26]. Present literature describes this behavior in terms of intrinsic material characteristics $G(t)$, $G'(\omega)$, $G''(\omega)$ [22, 23] which we use to generate their force connection analogs. In component design, these measures are related to $K(t)$, $K'(\omega)$, and $K''(\omega)$ by geometric factors. The critical gel behavior is described by the power-law equation:

$$K(t) = S_k t^{-n} \tag{3.17}$$

where S_k, dimensions $\left[\frac{F}{L} \cdot T^n\right]$, is the gel strength parameter and n is the power-law coefficient. The exponent is generally restricted to the range $0 < n < 1$, though is $n \approx 1/2$ for stoichiometrically balanced gels [22]. The dynamic moduli for the critical gel can be generalized to an extrinsic force connection as [22–24]:

$$K'(\omega) = \frac{K''(\omega)}{\tan\left(n\frac{\pi}{2}\right)} = \Gamma(1-n)\cos\left(\frac{n\pi}{2}\right) S_k \omega^n \tag{3.18}$$

where $\Gamma(\cdot)$ is the Gamma function. The first equality of Eqn. (3.18) links stiffness and damping, further constraining viscoelastic properties differently than assumed in the previous section. Note that $K''(\omega)$ and $K'(\omega)$ have equal slope for a given n (i.e., the modulus lines are parallel). Importantly, there is no simple mechanical analog with springs and dashpots for the critical gel (it requires an infinite set of parallel Maxwell elements). Yet, this behavior is accessible with real materials, if not (overly simplified) spring and dashpot

models.

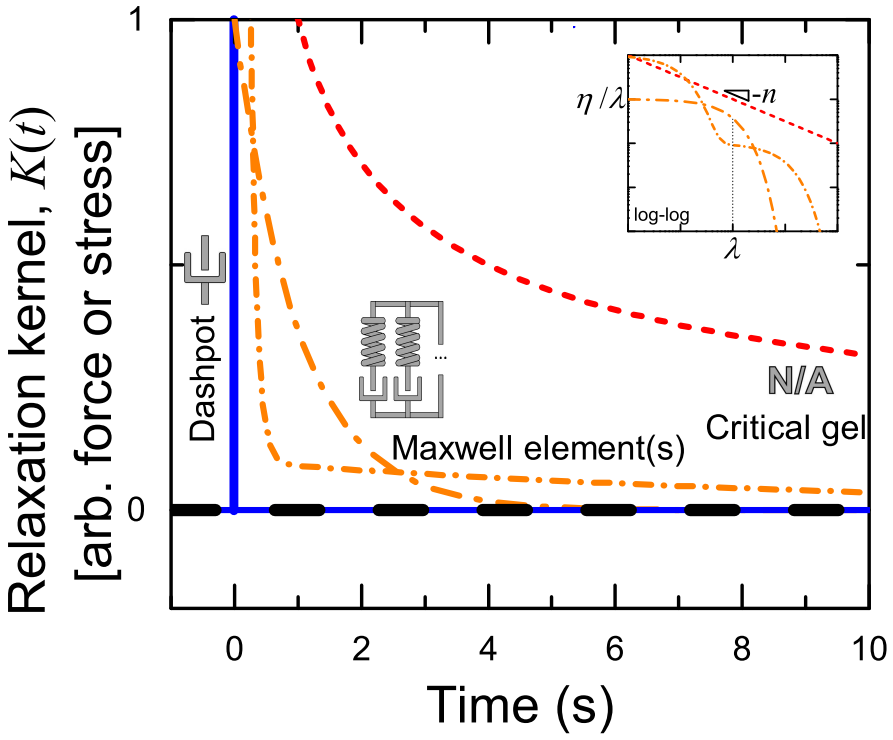

Figure 3.1: Parameterizations of the relaxation kernel, $K(t)$, for a general linear viscoelastic fluid model into numerous linear viscoelastic models to reduce the complexity of the design space. The viscoelsatic models used to parameterize the relaxation modulus of the added viscoelastic component are: (i) a linear dashpot (solid), (ii) a Maxwell element (linear spring and dashpot connected in series) single mode (dash-dot), (iii) Multi-mode Maxwell element, (short dash-dot), and (iv) a critical gel model, mechanical spring-dashpot analog is not applicable (dash). Inset plot is double-log plot of the same curves with the Maxwell model characteristic timescale λ (as in Eqn. (3.14)) and the critical gel exponent n (as in Eqn. (3.17)) labeled for reference [27].

While some parameterizations (i.e., Maxwell model) imply the use of a specified topology of linear springs and dashpots, this is not generally necessary for a viscoelastic connection. One could also parameterize $K(t)$ as a spline, or a discrete vector of independent points. This would be the ideal approach, with maximum design freedom, which is discussed in the following sections.

3.3 Generalized viscoelastic model

In the most general case, the optimization problem considered here seeks to minimize an objective function that describes the performance of the overall system and depends on the choice of $K(t)$. Since the optimization is performed with respect to $K(t)$, which is a function-valued design variable, this problem would fall under the class of optimal control problems [28]. While there are well-established methods to solve these types of problems [29, 30], the structure arising from the problem is complex due to the characteristic convolution integrals and is not yet well understood.

While previous studies have addressed viscoelastic material design, many have excluded the important feature of frequency dependence, resulting in limited design freedom, and thus do not capitalize on the valuable ability of viscoelastic materials to adjust properties with changes in loading frequency [31]. Other work involves time dependent behavior, but specifies that the linear viscoelastic functions be described by a superposition of exponential functions [32, 33]. The rigidity of this functional form limits the design space and will require large numbers of parameters. For example, using a discrete topology as shown in Fig. 3.2, restricts design freedom. This can be addressed by the introduction of a generalized viscoelastic element which makes the design space continuous. To implement an early-stage approach that supports more flexible design exploration, we consider a linear viscoelastic element where general mechanical response is described by experimentally measurable material functions that depend only on a timescale, the relaxation kernel, $K(t)$. Overall system performance can then be optimized by considering $K(t)$ as the design variable. The optimal function $K(t)$ can then serve as a target function in efforts to formulate a material that leads to optimal system performance.

Considering one-dimensional deformation as mentioned in Eqn. (3.19), we have:

$$F_{VE}(t) = \int_0^\infty K(s)\dot{x}(t-s)ds. \tag{3.19}$$

The convolution integral in Equation 3.19 presents a numerical challenge in optimization since the instantaneous state variables of the system cannot be represented by independent derivative functions, as the integral is not separable. In this thesis, we focus on the case where $K(t)$ is a general con-

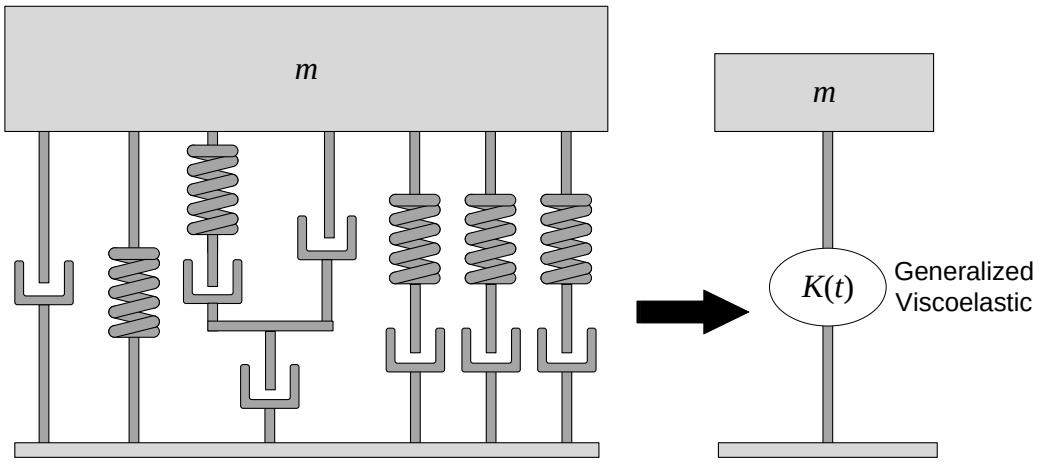

Figure 3.2: A discrete topology can be generalized by the introduction of a viscoelastic element.

tinuous function (i.e., no assumptions on the structure or parameterization of $K(t)$, as has been done in previous studies). For general relaxation kernels, evaluation of $F_{VE}(t)$ requires numerical solution. This force will appear in the governing differential equations for a dynamic system involving such a viscoelastic element. Because this convolution integral depends on complete past state histories it cannot be eliminated by adding a state variable to the system equations, and thus results in a system of integro-differential equations.

Without special structure of $K(t)$, there is not a closed-form solution for the convolution integral or the system differential equations. Thus, solving for state trajectories will require numerical simulation of the differential equations, and numerical solution of the convolution integral every time the time derivative function for the differential equations must be evaluated. This is a computationally intensive process, particularly if coupled with optimization (i.e., for every optimization function call a simulation must be performed, and for every derivative function evaluation made during simulation the convolution integral must be solved numerically). In the following section we review the mathematical nature of integro-differential equations, their solution methods, and the physical systems they are associated with.

3.4 Integro-Differential Equations (IDEs)

Integro-differential equations are, as the name suggests, equations that contain both an integral and derivative terms. They typically fall in one of the two categories [34]:

1. Volterra integro-differential equations of the form:

$$\phi(x)u''(x) = f(x) + \lambda \int_a^x K(x,t)u(t)dt \tag{3.20}$$

2. Fredholm integro-differential equations of the form:

$$\phi(x)u''(x) = f(x) + \lambda \int_a^b K(x,t)u(t)dt \tag{3.21}$$

Specifically, if the kernel function $K(x,t)$ in Eqn. (3.20) is of the form $K(x-t)$, then the integral is classified as a convolution integral (as is the case with Eqn. (3.19)). One must note that the derivative term can exist within and/or outside of the integrand in an integro-differential equation. The system model corresponding to a linear viscoelastic element is a Volterra IDE.

Many solution methods for IDEs have been explored in the literature. The Laplace transform is often used when the structure of the kernel function is known. Other traditional methods include the series solution method where a Volterra IDE is converted to an initial value problem or a Volterra integral equation [35]. Once the IDE is converted to an integral equation, there exist a multitude of methods to solve the system [36, 37]. Brunner surveyed various numerical techniques that can be applied to IDEs [38] and applied Runge-Kutta methods to second-order IDEs [39] and detailed the use of finite element methods to solve optimal control problems consisting of IDEs [40]. Other work included quadrature methods to solve Volterra and Abel-Volterra equations [41]. Dixon studied multistep methods used in the solution of Volterra integral and integro-differential equations of the second kind [42]. Other methods to solve higher-order and non-linear IDEs that have been studied are the power series method [43], Adomian Decomposition method [44, 45] and its modifications [46, 47]. The Variational Iteration Method (VIM) has also been used to solve non-linear IDEs numerically [48].

Jiang et al. propose a convolution integral method to simulate real-time hybrid systems [49]. Edwards analysed the numerical simulation of Volterra IDEs [50]. Most of these efforts, however, do not focus on convolution kernel solution or using IDEs in conjunction with engineering design optimization.

3.4.1 Modeling Convolution Kernels in IDEs

Several methods of convolution quadrature have been studied, which is important for numerical evaluation of hysteretic systems. Lubich, a pioneer of the convolution quadrature, uses Laplace transforms to determine quadrature weights [51]. Lubich et al. also applied quadrature to fractional IDEs [52]. However, in these cases the structure of the kernel functions $K(x-t)$ was known a priori. Zhang et al. proposed using a combination of linear methods with compound quadrature rules [53]. Finite elements were also used for this purpose when the system involved modeling of flow and partial differential equations [54, 55]. These efforts form a strong mathematical basis to understand convolution kernels and IDEs, but in general do not address rate-dependent convolution kernels of the form given in Eqn. (3.19), and do not extend their use in engineering design optimization.

In this thesis we introduce the use of optimal control in the optimization of viscoelastic systems (characterized by convolution IDEs), specifically for the case of general relaxation kernels $K(t)$. Optimal control methods have successfully been used in the optimization of similar systems, such as wave energy converters [56] where the cost functional term has a rate-dependent convolution structure. Yu and Falnes approached the problem by using a state space approximation of the convolution term; this approximation results in additional system model states [57]. The objective of this study is to identify a generalized form of the shear relaxation modulus $K(t)$ found in Eqn. (3.19) to support more flexible design strategies for early-stage design exploration involving viscoelastic materials. This flexibility may help reduce design fixation and enhance design innovation using rheologically complex materials.

3.5 Optimal Control methods

The desired early-stage design approach that is not restricted by a priori material class choices (i.e., material agnostic) requires a generalized treatment of $K(t)$. Instead of parameterizing $K(t)$ and tuning parameters to improve system performance, we propose to design $K(t)$ directly. In other words, instead of specifying a finite set of parameters as design variables, we choose to design with respect to an infinite-dimensional (function-valued) quantity. Optimal control methods provide the ability to solve infinite-dimensional optimization problems.

Optimal control is a mature field of study [58]. An optimal control system design (OCSD) problem aims to find a state trajectory $\boldsymbol{\xi}(t)$ and a control trajectory $\mathbf{u}(t)$ that satisfy system dynamics relationships and maximize system performance. In general, an optimal control problem can be formulated as follows [59]:

$$\begin{aligned} \min_{\mathbf{x}} \quad & \int_{t_0}^{t_f} \mathcal{L}\left(t, \boldsymbol{\xi}(t), \mathbf{x}\right) dt + \mathcal{M}\left(t, t_0, \boldsymbol{\xi}(t_0), t_f, \boldsymbol{\xi}(t_f), \mathbf{x}\right) \\ \text{subject to} \quad & \dot{\boldsymbol{\xi}} = \mathbf{f_d}(t, \boldsymbol{\xi}(t), \mathbf{x}), \\ & \mathbf{C}\left(t, \boldsymbol{\xi}(t), \mathbf{x}\right) \leq \mathbf{0} \\ & \boldsymbol{\phi}\left(t_0, \boldsymbol{\xi}(t_0), t_f, \boldsymbol{\xi}(t_f), \mathbf{x}\right) \leq \mathbf{0} \end{aligned} \tag{3.22}$$

where $\mathbf{x}$ is the set of optimization variables, which can include state variable trajectories $\boldsymbol{\xi}(\cdot)$, control input trajectories $\mathbf{u}(t)$, and initial (t_0) or final time (t_f). $\mathbf{f_d}(\cdot)$ is the time derivative function for the state equations that describe system dynamics. $\mathbf{C}(\cdot)$ is the path constraint function, and $\boldsymbol{\phi}(\cdot)$ is the boundary constraint function. $\mathcal{L}(\cdot)$ is the Lagrangian that quantifies the running cost portion of the objective function, and $\mathcal{M}(\cdot)$ is the objective function term that depends on boundary values.

The OCSD problem aims to design a trajectory for the state and/or control variables that minimizes a Lagrangian cost function $\mathcal{L}(\cdot)$, while satisfying the constraints $\mathbf{C}(\cdot)$ and $\boldsymbol{\phi}(\cdot)$.

In drawing parallels to the viscoelastic problem at hand, we make certain observations. The independent control input $\mathbf{u}(t)$ is analogous to the shear relaxation modulus $K(t)$ and the OCSD problem aims to find a $K(t)$ that minimizes the objective function. The objective cost function $\mathcal{L}(\cdot)$ can be any

function of the state and control variables. For instance, in its use in vibration damping, the objective of the OCSD problem could be to minimize the peak amplitude of displacement. The state trajectories $\boldsymbol{\xi}(t)$ in this example could be the displacement or velocity vectors. $\mathbf{f_d}(\cdot)$ represents the system dynamics of the viscoelastic system and would include the viscoelastic force described in Eqn. (3.19). One may have boundary constraints on the initial and final states of the system. Path constraints may exist when the state or control trajectories are required to follow a target trajectory shape. This might be relevant in the case of designing a physically realizable $K(t)$.

3.5.1 Solution Methods for Optimal Control System design

This subsection discusses the solution methods adopted for OCSD problems. Following a brief insight into these methods, we will discuss the key differences between the standard OCSD problem and the viscoelastic design problem. There are two classes of methods employed to solve OCSD problems: (1) indirect and (2) direct optimal control methods.

Indirect Optimal Control

Indirect methods are based on the calculus of variations, and work by applying optimality conditions to the optimal control problem to form a boundary value problems (BVP). In simple cases the BVP may be solved analytically, but in more general cases it must be discretized and solved numerically [60]. The general algorithm of an indirect method is optimize-then-discretize ($O \rightarrow D$).

Indirect approaches help provide insights into the structure of the solution, but usually the analytical derivatives are challenging to calculate. In the case of expensive or black-box functions, derivatives are numerically calculated.

Direct Optimal Control

Direct optimal control methods take the opposite approach, where the optimal control problem is discretized in time first, i.e. discretize-then-optimize ($D \rightarrow O$). The result is a nonlinear program (NLP) that can be solved using

standard large-scale optimization algorithms. Direct methods are particularly effective for highly nonlinear systems, problems with inequality constraints, or other situations where indirect methods fall short [29, 30]. The state space equations are discretized to form a system of algebraic equations (known as defect equations or defect constraints, similar to residual functions). This discretization makes use of a collocation method (e.g., implicit Runge-Kutta [61]). A number of different direct methods exist broadly classified as sequential and simultaneous. Sequential approaches only parameterize control while simultaneous approaches parameterize both control and state.

Single Shooting - The most straightforward of the direct methods is single-shooting where the state trajectories are obtained for every NLP function evaluation by solving the defect equations using forward simulation. Thus, single shooting is an example of a sequential direct optimal control method. The control is parameterized by using either a polynomial approximation or another appropriate method. Given a set of initial conditions and control parameters, the optimization is then performed with respect to the control parameters (or polynomial coefficients). While single-shooting can ensure feasibility and optimality, it requires the simulation of the OCSD problem for every function call of the optimization algorithm, making it numerically cumbersome.

Multiple Shooting - Multiple shooting separates the time horizon into smaller segments and separate models are built on these segments. Continuity constraints are required in between two consecutive segments. This ensures more robustness and is better at handling instabilities.

Sequential methods face difficulties in handling boundary and path constraints that often lead to inaccurate and computationally inefficient solutions [62], motivating the need to move to simultaneous approaches.

Direct Transcription - Simultaneous methods, also called Direct Transcription (DT), parameterize both control and state. They construct an large NLP problem and do not require nested simulations. The new NLP now has a sparsity structure (in the form of a state space matrix) that can be exploited to reduce the total computational expense. DT can be classified into local and global collocation methods. In local collocation, a time-marching method with a low polynomial order such as Euler, Trapezoidal etc., is used in discretization. Global collocation methods use higher degree pseudospec-

tral methods that result in a higher accuracy [59].

It is easy to make observations on the similarities between the standard OCSD problem and the viscoelastic formulation. However it is important to understand the subtle differences that exist in the viscoelastic problem. As discussed in the previous sub-section, the convolution integral poses significant challenges in the modeling of viscoelastic material based systems. One place where this challenge shows up is in the structure of the OCSD problem. With the use of the viscoelastic element, the viscoelastic force in Eqn. (3.19) typically appears in the derivative function equation, $\mathbf{f_d}(\cdot)$. Discretizing F_{VE} in time using a convolution sum would result in:

$$F_{VE}[k] = \int_0^{t_k} K(s)\dot{x}(t-s)ds = \sum_{i=0}^{k} K[i]\dot{x}[k-i+1] \tag{3.23}$$

where k denotes the k^{th} time step representing the time instant t_k. We can see from this discretization that we would require a summation of F_{VE} over all the time instants prior to t_k. This is atypical of a standard optimal control problem, where the states and derivative functions usually depend only on the current and the immediate previous time-step.

Another subtle difference is in the direction of the time marching between the state and control. Usually, in a standard OCSD problems, both state and control march forward in time. In the viscoelastic problem we can see that the control, $K(t)$ and the state, $\dot{x}(t)$, *convolve* in time. In graphical terms, the convolution of teo functions f and g, is written as $f * g$. It is defined as the integral of the product of the two functions after one is reversed and shifted. For example, consider the convolution of the unit impulse function with the exponential function:

$$f(t) = u(t) \tag{3.24}$$

$$g(t) = e^{-t}u(t) \tag{3.25}$$

where

$$u(t) = \begin{cases} 1 & : t \geq 0 \\ 0 & : t < 0 \end{cases}$$

The convolution of the two functions is given by:

$$f * g = \int_{-\infty}^{\infty} f(\tau)g(t-\tau)d\tau \tag{3.26}$$

As a first step $g(t)$ is reversed and then shifted. For $t < 0$ there is no overlap between $u(\tau)$ and $u(t-\tau)$. Thus the convolution can be rewritten as:

$$f * g = \int_{0}^{t} f(\tau)g(t-\tau)d\tau = e^{-t}\int_{0}^{t} e^{\tau}d\tau = 1 - e^{-t} \tag{3.27}$$

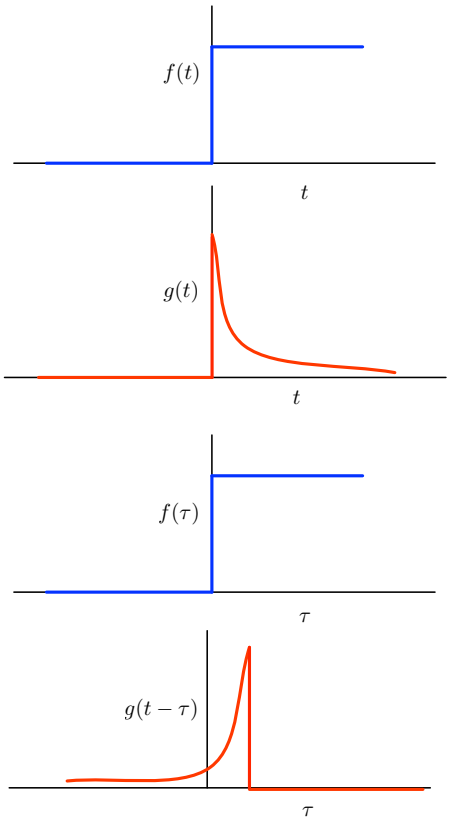

Figure 3.3: $f(t)$ is convolved with $g(t)$ by reversing and shifting $g(t)$

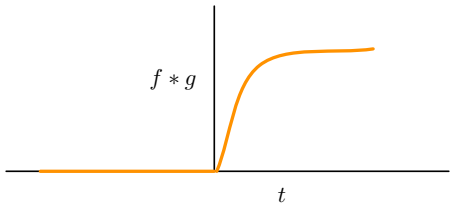

Figure 3.4: The result of the convolution

As we can see from the simple example of convolution shown above, the viscoelastic problem has a convolution of the control, i.e. $K(t)$ and the state, i.e. $\dot{x}(t)$. This implies that it requires one of the functions to be reversed and shifted, which is not a standard case of an optimal control problem, where the control and state are marched forward in time simultaneously. With this introduction to both model-based and optimal control-based approaches, we will now dive into the specifics of a vibration isolator problem.

CHAPTER 4

Numerical Studies on a vibration isolator - Part 1

In this chapter, the use of viscoelastic materials in engineering design is demonstrated with a case study involving a vibration isolator design. Initially, the study is conducted using existing viscoelastic models such as Maxwell, Critical Gel and the optimal paramters of design are identified for each viscoelast model. In Chapter 5, the study is then extended to entail generalized viscoelastic design, free from parameterizations and optimal control methods are utilized in the optimization of this system.

4.1 Case study

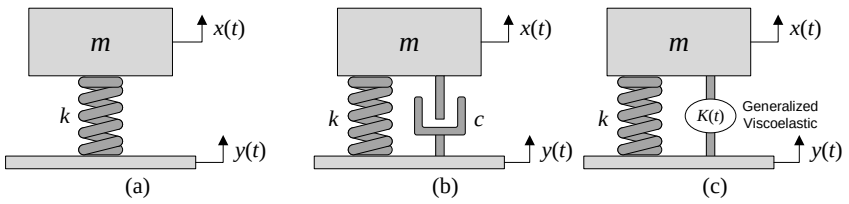

Figure 4.1: Design of optimal viscoelastic vibration isolation for a 1-dimensional spring-mass system(a); (b) the typical approach of an arrangement of springs and dashpots, and (c) a generalized viscoelastic element with relaxation kernel, $K(t)$. The latter approach increases design freedom and identifies more optimal targets.

In general, the linear viscoelastic element described in Chapter 3, could be used to connect any two pieces in a system. As a case study, we consider a simple vibration isolator, shown in Fig. 4.1. In the initial case (Fig. 4.1.a), a mass m is connected by a spring to a base that is moving with a prescribed displacement of $y(t)$. The objective is to isolate the top mass from the base displacement. A simple improvement is the addition of a linear dashpot

(Fig. 4.1.b). We will generalize the linear dashpot to be a parallel viscoelastic connection with relaxation kernel $K(t)$, described in Chapter 3. We will demonstrate the added performance from a viscoelastic connection (shown in Fig. 4.1c), and optimize $K(t)$ based on the parameterizations described in Sec. 3.2.

4.1.1 Governing Equations

Given an initial condition $F_{ve}(t=0)=0$, Eqn. (3.19) has limits of integration from 0 to t. In general, the expression requires convolution of the kernel function $K(t)$ with the entire time-history of the velocity experienced by the element, $\dot{x}(t)$.

For the particular system in Fig. 4.1.c, with a generalized viscoelastic element and the initial condition $F_{ve}(t=0)=0$, the governing equation for conservation of linear momentum is most generally written as:

$$-k(x-y)-\int_0^t K(s)\left[\dot{x}(t-s)-\dot{y}(t-s)\right]ds = m\ddot{x}(t) \tag{4.1}$$

where $s=t-t'$ and $\dot{x}-\dot{y}=\dot{X}$, or the velocity of deformation, as defined in Eqn. (3.19).

The convolution integral structure has two important consequences. First, the equations cannot be written in matrix form. Second, the numerical simulation of this model requires increased computation at each time step, since each time derivative function evaluation requires an integration of the entire prior time-history of velocities. This is an important challenge to be addressed for general design of $K(t)$, and is discussed in Chapter 5. Here, we simplify the analysis by considering time-periodic solutions for which the convolution integral simplifies. Consider a time-periodic prescribed base excitation, $y(t)=Y\sin(\omega t)$. For a linear system, the steady-state displacement response of $x(t)$ will be time-periodic at the forcing frequency [63]. The known structure of this harmonic solution will simplify the convolution integral terms, to an extent that we *can* write the governing equations as a function of instantaneous state variables. Thus, integral calculations of $K(t)$ terms are not required at each time step.

Using complex notation, the displacement of the mass has the form:

$$x(t) = \text{Im}\left\{x^* e^{i\omega t}\right\} \tag{4.2}$$

where Im{} takes the imaginary portion of the complex quantity. The coefficients are:

$$x^* = X_R + iX_i \tag{4.3}$$

By substituting Eqns. (4.2) and (4.3) into Eqn. (4.1), a linear system of two equations and two unknowns will result. The system of equations takes the form:

$$\mathbf{Mx} = \mathbf{B}. \tag{4.4}$$

The unknowns are

$$\mathbf{x} = [X_R, X_i]^{\mathrm{T}} \tag{4.5}$$

The nonhomogeneous portion is:

$$\mathbf{B} = [-Y(\omega S + k), -Y\omega C] \tag{4.6}$$

and the 2 by 2 matrix is given by:

$$\mathbf{M} = \begin{bmatrix} (m\omega^2 - \omega S - k) & (\omega C) \\ (-\omega C) & (m\omega^2 - \omega S - k) \end{bmatrix} \tag{4.7}$$

The scalar coefficients C and S require integral calculations that depend on the kernel function $K(t)$,

$$C(\omega) = \int_0^\infty K(s)\cos(\omega s)ds \tag{4.8}$$

$$S(\omega) = \int_0^\infty K(s)\sin(\omega s)ds. \tag{4.9}$$

Comparing this result to Eqn. (3.6) and Eqn. (3.7) shows that these integrals are related to the dynamic material functions as

$$C = K''(\omega)/\omega \tag{4.10}$$

$$S = K'(\omega)/\omega. \tag{4.11}$$

The primary design variable is still $K(s)$, since it gives the rheological signa-

ture of both dynamic moduli, and the dynamic moduli are not independent parameters due to the Kramers-Kronig relations in Eqn. (3.9).

The solutions to the governing equations give $|x|$, the displacement amplitude of the mass, as a function of frequency. Normalizing this result by the input displacement amplitude, Y, leads to the non-dimensionalized amplitude.

$$|\tilde{x}| = \frac{|x|}{Y} \tag{4.12}$$

From the displacement, the acceleration amplitude of the mass is defined to be:

$$|\ddot{x}| = \omega^2 |x| \tag{4.13}$$

Equivalently, it can be non-dimensionalized by the problem inputs of dispalcement ($Y \doteq [length]$), mass ($m \doteq [mass]$), and spring constant ($k \doteq \left[\frac{mass}{time}^2\right]$) as:

$$|\tilde{\ddot{x}}| = \frac{|\ddot{x}|}{Y\left(\frac{k}{m}\right)} \tag{4.14}$$

In general $K(t)$ can take any form, but here $K(t)$ is parameterized using the methods described in Section 3.2. The response $\tilde{\ddot{x}}$ is optimized by minimizing the peak value with respect to a finite set of design variables that parameterize $K(t)$. These parameters can themselves be non-dimensionalized as follows. For the linear dashpot, $\tilde{c} = {}^{c}/\sqrt{km}$; for the Maxwell model, $\tilde{\lambda} = {}^{\lambda}/\sqrt{m/k}$ and $\tilde{\eta} = {}^{\eta}/\sqrt{km}$; and for the critical gel, $\tilde{S} = {}^{S}/\frac{k^{\frac{1}{2}(2+n)}}{m^{n/2}\frac{1}{Y}}$ (note that the critical gel exponent, n, is dimensionless).

The objective function f for the design optimization problem here is the maximum non-dimensionalized acceleration amplitude.

$$f(x) = \max |\tilde{\ddot{x}}| \tag{4.15}$$

4.2 Results

Relaxing the design space to include even simple parameterizations of viscoelastic fluids can change the behavior of the vibration isolator, as demonstrated in Fig. 4.2. While parametrization does not provide infinite design freedom, it is valuable for this initial treatment, as it allows a visualization of the extended design space. A Maxwell model allows for the introduction

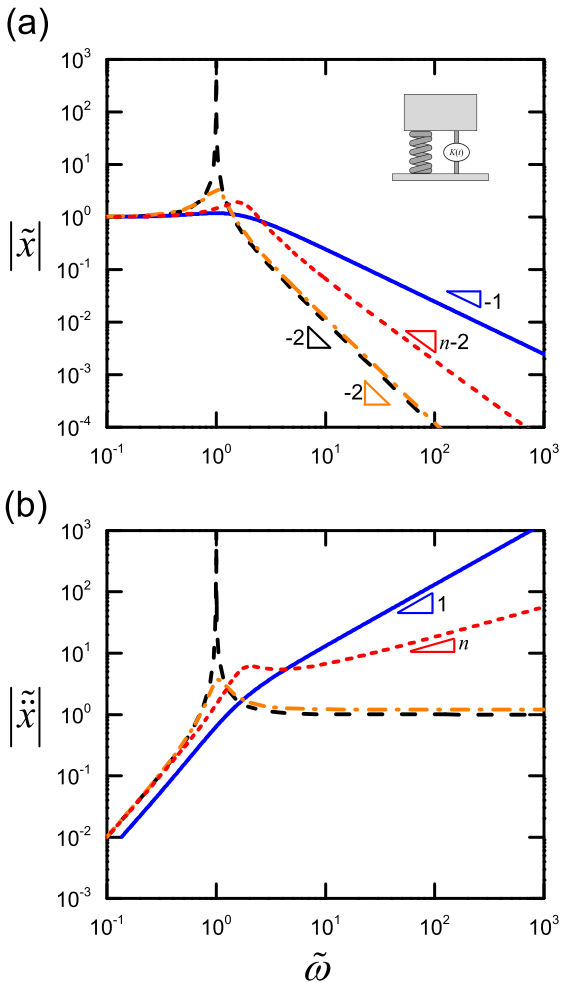

Figure 4.2: Design involving a generalized viscoelastic element with relaxation kernel $K(t)$ can eliminate high frequency acceleration. Here shown with Maxwell element (dash-dot), and critical gel (short dashed) compared to dashpot (solid), or no additional component (dashed) [27].

of an additional timescale, λ from Eqn. (3.14); for characteristic deformation timescales longer than λ where the connection (or material) behavior transitions from spring-like (elastic) to dashpot-like (viscous). The high-frequency (short timescale) elastic behavior is a key feature. Properly designed, this allows for an attenuation of the peak acceleration at a resonant frequency *without* the penalty of ever-increasing acceleration at large ω. This is illustrated in Fig. 4.2. Note $\tilde{\omega} = \omega/\omega_{res}$, where ω_{res} depends on the Maxwell parameters. Other parameterizations likewise allow for reduction of the resonant acceleration with reduced penalty at high frequencies.

Table 4.1: Optimized peak acceleration and corresponding viscoelastic design for a simple vibration isolator. Accelerations and parameters are non-dimensionalized according to Section 4.1.1.

VE Model	**Peak Acceleration** $\lvert\tilde{\ddot{x}}\rvert$	**VE Parameters**
Dashpot	309.67 ± 0.000	$\tilde{c} = 0.00155 \pm 0.00000$
Maxwell Element	3.001 ± 0.004	$\tilde{\eta} = 0.553 \pm 0.011$; $\tilde{\lambda} = 0.277 \pm 0.005$
Multi-mode Maxwell ($m = 3$)	3.000 ± 0.000	see text
Critical Gel	10.755 ± 0.026	$\tilde{S} = 0.046 \pm 0.037$; $n = 0.259 \pm 0.008$

We optimized the different forms of the kernel function to minimize the peak acceleration of the mass m. Optimization was performed using the MATLAB™ optimization toolbox with the functions '`ga`' and '`fmincon`'. In order to ensure a global minimum, a hybrid solution approach is used. This is achieved by optimizing the objective function first using '`ga`', which is a global search algorithm. The optimization variables obtained from '`ga`' are then fed into '`fmincon`' as a starting guess. The results for the optimal viscoelastic kernel functions are presented in Table 4.1.

In the case of a multi-mode Maxwell model, the optimized viscoelastic parameters are not listed in Table 4.1, since there was too much variation in the individual values. However, all values for η and λ produced similar $K(t)$ curves (in addition to being similar to the single mode Maxwell model). This shows that the shape of the curve is the key factor in optimization, not its exact parametrization.

The peak amplitude can occur either as a local maximum near resonance (e.g., Fig. 4.2, critical gel), or at the highest frequency considered (e.g., Fig. 4.2, dashpot). Therefore, some solutions depend on the frequency range of interest. Shapes of all optimized $K(t)$ curves are shown in Fig. 4.3. For both the dashpot and critical gel, the acceleration amplitude increases without bound at higher frequency, thus increasing the upper-bound of the frequency range will increase the acceleration amplitude at that value, possibly above the local peak value at the resonant frequency. For real applications

a finite range of frequency is reasonable, e.g., excitation amplitudes decrease and may be negligible above a critical frequency.

Introducing a linear viscoelastic connection decreases the peak acceleration beyond that of a simple linear dashpot. With the introduction of a characteristic timescale, a Maxwell model provided the most improvement compared to the conventional method. A critical gel element also provides a marked improvement. Surprisingly, in this simplified problem, additional design freedom in the form of additional viscoelastic parameters (i.e. a multi-mode Maxwell model) does not provide further improvement over a single mode Maxwell model. This is likely due to the fact that this toy problem has only one characteristic frequency, thus only one additional time scale is necessary for optimal performance.

These results suggest that a critical gel model and multi-mode Maxwell model may further improve performance for more complex problems involving a more complicated forcing function. More degrees of freedom and additional characteristic timescales may prove beneficial in excitations that superpose multiple frequencies, or structures with multiple vibration modes.

4.2.1 Case Study Extension

As an extension to the above results and in order to get a better intuition for more practical systems, the dynamic vibration isolator was further generalized to consider a range of non-dimensional natural frequencies $\tilde{\omega}^*$ for which a single viscoelastic element is used. This natural frequency is normalized by some reference spring-mass system (k_0, m_0) such that:

$$\tilde{\omega}^* = \frac{\omega^*}{\omega_0} \tag{4.16}$$

where ω_0 is the natural frequency of the reference system $\omega_0 = \sqrt{k_0/m_0}$.

This is analogous to a "one size fits all" damper where the primary mass and spring may vary by application (Fig. 4.4). As shown before, use and optimization of a generalized viscoelastic element for a fixed natural frequency (i.e. $\tilde{\omega}^* = 1$), significantly improves the system response. However, the benefit of the optimized viscoelastic element is diluted for a system whose natural frequency is different from that for which the system is optimized.

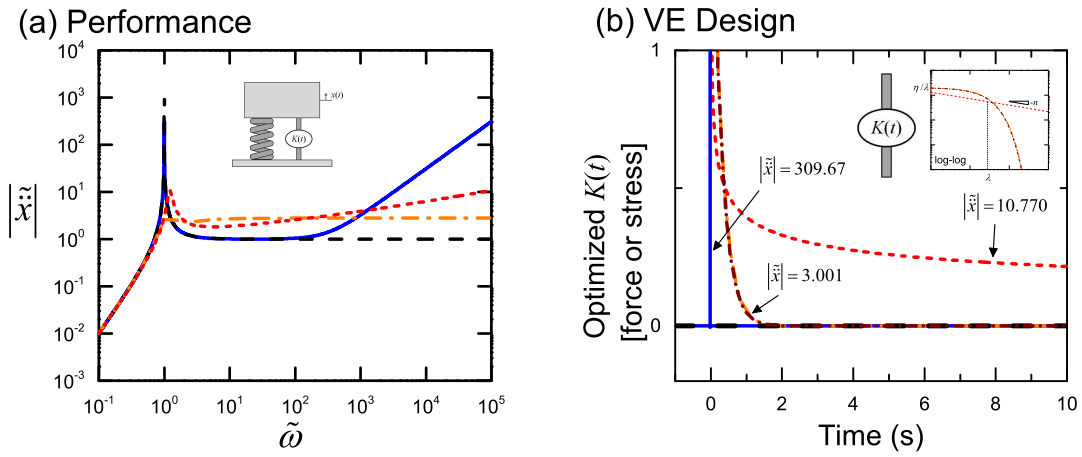

Figure 4.3: Optimized performance (acceleration amplitude), left, and the corresponding optimal viscoelastic design (kernel function), right. The viscoelastic models used to parameterize the relaxation kernel of the added viscoelastic component (shown in Fig. 4.1c) are: (i) a linear dashpot, solid, (ii) a single mode Maxwell element, dash-dot, (iii) Three-mode Maxwell element, short dash-dot, (iv) a critical gel model, short dashed, and (v) no additional component, dashed. A multi-mode Maxwell model only uses its additional degrees of freedom to achieve the same relaxation kernel and performance as a single mode, which therefore overlap as the most optimal of these parameterizations.

In practice, it is unlikely that a system will be as idealized as the simple spring-mass isolator system proposed in the previous case study. A simple example can be thought of as a vehicle suspension system, where the vehicle is expected to perform over a wide range of additional mass. By extending the original example to include a range of natural frequencies, we allow for the possiblity of added mass or a range of system stiffness.

For the previous studies with a fixed $\tilde{\omega}^* = 1$, the objective function was chosen to be the maximum of the acceleration curve. Now, with a range of natural frequencies, selecting the absolute maximum would result in a a discontinuous and non-smooth objective function. To avoid problems associated with discontinuities, the following (similar) objective function was used instead:

$$f(x) = \left[\sum_{\omega_{1i}}^{m} \max(\ddot{X}_i)^n\right]^{1/n} \tag{4.17}$$

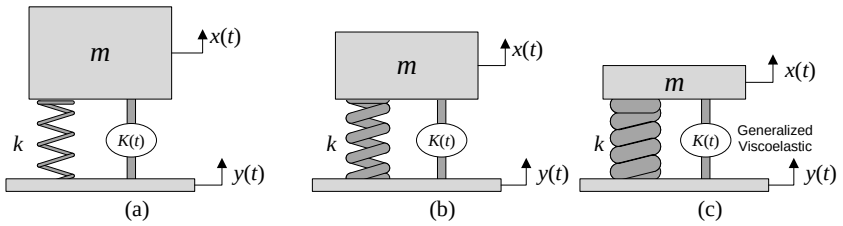

Figure 4.4: The simple vibration isolator problem is extended to optimize the performance for a range of natural frequencies of the system, but a fixed $K(t)$. Increasing the natural frequency of the system ($\omega_1 = \sqrt{k/m}$) can be conceptualized by increasing the spring constant k and/or decreasing the system mass, m, shown in (a)-(c).

where the non-dimensional frequency increases and decreases by an order or magnitude, i.e. $\tilde{\omega}^* \in \{0.1, 1, 10\}$ and $\ddot{X}_i$ refers to the corresponding acceleration versus frequency curve for each $\tilde{\omega}^*$.

Equation (4.17) is the nth norm of the acceleration peaks over a range of natural frequencies. It becomes essential to assign a reasonable value for n so that the objective function adequately weighs the cost of a high peak in acceleration. Here n is chosen to be 4. The results from this optimization formulation are discussed below.

The Maxwell model and critical gel model were both used within this new optimization scheme. The dashed lines in Fig. 4.5 show the system design (right) and performance (left) over a range $\tilde{\omega}^*$ optimized for a reference natural frequency ($\tilde{\omega}^* = 1$). While the response of the $\tilde{\omega}^* = 1$ system is obviously optimized, the system as a whole is problematic. In the case of the Maxwell element, the time scale optimized for this natural frequency (shown as the dotted vertical line in Fig. 4.5a) matches the resonance peak with the high-frequency plateau behavior. However, this characteristic timescale is too long (i.e., the frequency is too low) to prevent an increased high-frequency plateau should the system have a lower natural frequency. Likewise, the timescale is too short to effectly attenuate the resonance peak for a system of a higher natural frequency. The extended optimization problem takes these trade-offs into account and is able to effectively match the most significant high frequency component ($\tilde{\omega}^* = 0.1$ rad/s) with the most significant resonance acceleration ($\tilde{\omega}^* = 10$ rad/s), leading to a design that is optimized in a more balanced manner, reducing the objective function by 32%.

Likewise, the critical gel model optimized for the reference natural frequency ($\tilde{\omega}^* = 1$) leads to problems with high frequency behavior for lower natural frequencies and resonance attenuation for higher natural frequencies. Optimizing for the entire range of natural frequencies allows for improved overall results for the system, as shown in the solid lines of Fig. 4.5. The objective function is decreased by 51%.

In both viscoelastic parameterizations, overall optimization of the system comes at a cost of higher maximum accelerations for some natural frequencies, shown as the circles along the non-dimensional acceleration axes in Fig. 4.5. Values of nondimensionalized acceleartion are shown in Table 4.2.

For the extension of the original case study, the maximum acceleration amplitude was reduced for both the single element Maxwell and critical gel models. As in the previous case study, the additional degrees of design freedom in the multi-mode Maxwell model provided no further improvement over a single mode. The full results of this extension are presented in Table 4.2.

Table 4.2: Optimized peak acceleration magnitudes and optimized viscoelastic parameters for the extended vibration isolator problem. Bolded values indicate the objective function for the optimizer [27].

Opt. For		**Maximum Acceleration**			**Fourth Norm**	**V.E. Parameters**
		$\tilde{\omega}^* = 0.1$	$\tilde{\omega}^* = 1$	$\tilde{\omega}^* = 10$		
Maxwell	$\tilde{\omega}^* = 1$	21.0	**3.00**	22.5	25.9	$\tilde{\lambda} = 0.277$ $\tilde{\eta} = 0.553$
	Range of $\tilde{\omega}^*$	15.4	7.57	15.5	**18.5**	$\tilde{\lambda} = 0.0952$ $\tilde{\eta} = 0.137$
Critical Gel	$\tilde{\omega}^* = 1$	99.9	**10.8**	32.3	100.2	$\tilde{S} = 0.406$ $n = 0.259$
	Range of $\tilde{\omega}^*$	33.1	17.7	42.5	**49.2**	$\tilde{S} = 0.246$ $n = 0.118$

The new optimization scheme dramatically affects the optimized kernel function shape, $K(t)$. The kernel functions optimized for a fixed natural fre-

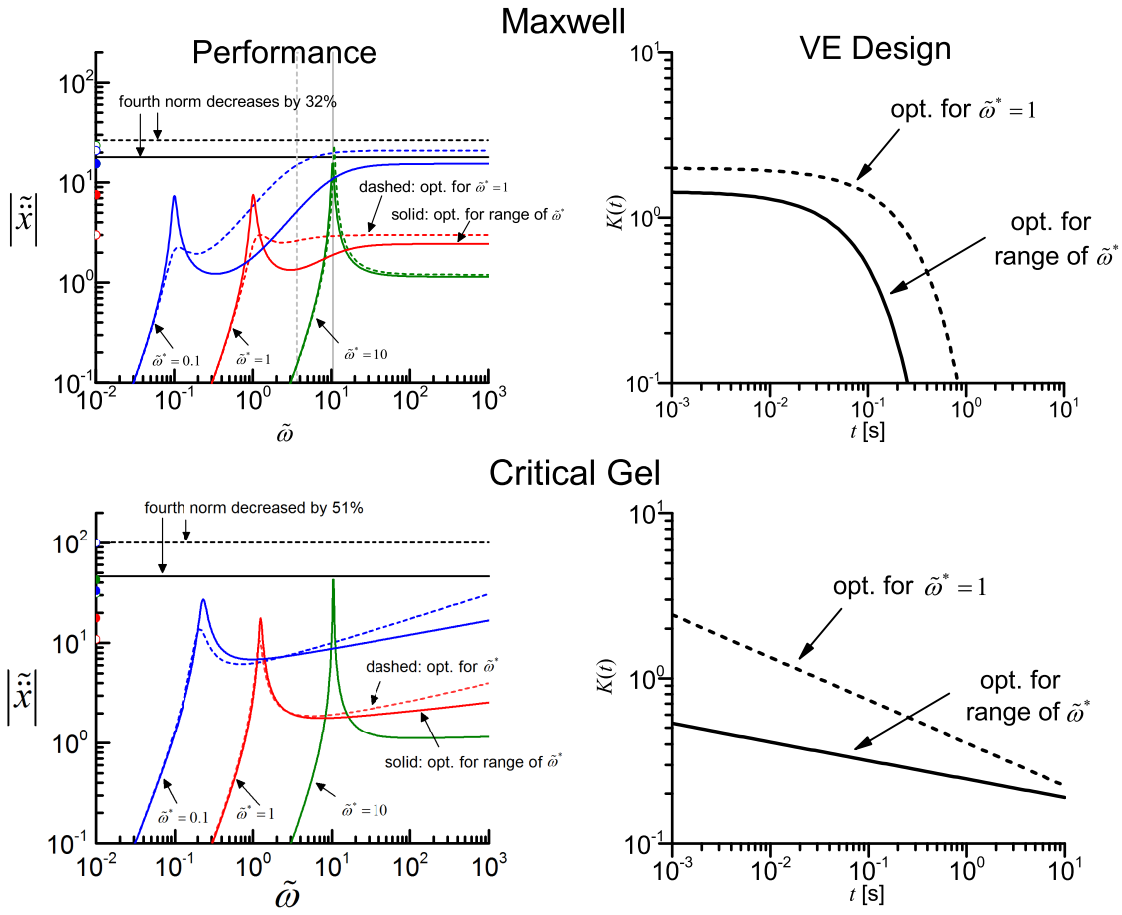

Figure 4.5: The performance (left) and viscoelastic design(right) for a Maxwell element and critical gel element in the extended vibration isolation problem. Multi-mode and single mode system response was identical, thus only a single mode is shown. The system performance is measured by the acceleration response while the viscoelastic design corresponds to the kernel function, $K(t)$, of the viscoelastic element. Dashed lines represent optimization for a reference non-dimensional natural frequency $\tilde{\omega}^* = 1$, where $\tilde{\omega}^*$ is as described in Eq. (4.16); solid lines represent the results optimized for the range of $\tilde{\omega}^*$. In the left panels (performance), the values of the objective function (fourth order norm of the maximum accelerations of each curve), optimized for a reference $\tilde{\omega}^* = 1$ (dashed) and a range of $\tilde{\omega}^*$ values are shown as horizontal black lines. The optimizer works to minimize this objective function [27].

quency and a range of natural frequency are shown in Fig. 4.5. The expanded range pushes the optimal characteristic timescale, λ, lower to improve the high-frequency behavior of the system. The range of frequencies decreases

the magnitude of n, the critical gel exponent, effectively making the system more solid-like, again improving the high-frequency behavior of the system.

An important note to make is that these results, even more so than the original problem, are dependent on the range of input frequency ($\tilde{\omega}$) chosen. The ever-increasing acceleration at high frequency for a liquid-like system as well as a critical gel model drives the optimized results.

Passive vibration isolators find use in a variety of practical applications. In their use as air isolators in large industrial equipment, the typical natural frequency range is 1.5-3 Hz. In the case of base isolators used in buildings and large structures, the natural frequency varies over a low seismic range. Their usage in vehicles and aviation pertains to a frequency range of 10-20 Hz. The key takeaway here is that real world vibration isolation occurs over not just one but a range of resonant frequencies, for which viscoelastic responses can be optimized.

Having established a good basis for using viscoelastic materials in a vibration isolator case study, we will now move on to generalizing the problem. This is achieved by freeing $K(t)$ of its model parameterizations and is discussed in detail in the upcoming chapter.

CHAPTER 5

Numerical Studies on a vibration isolator - Part 2

In the case study performed in the previous section, $K(t)$ was parameterized with the help of standard linear viscoelastic models. As a subsequent step, a more generalized form of $K(t)$ is utilized in the vibration isolator problem. By freeing $K(t)$ from a specific mathematical structure (such as a decaying exponential in the case of a Maxwell model), $K(t)$ becomes an infinite-dimensional design variable to the optimization problem described in Sec. 4.1. As discussed in Chapter 3, optimal control methods are best used in order to solve optimization problems with function-valued design or control variables. Thus, as the first step to achieving generalized viscoelastic design in the vibration isolator problem, we need to formulate the existing problem as an optimal control problem.

5.1 Formulation of the optimal control problem

In the optimal control problem formulation, we consider $K(t)$ to be the control input that we wish to design in order to minimize a certain objective. While treating $K(t)$ as a system control input is an intuitive solution strategy, the convolution structure of the problem presents some challenges. The integral corresponds to the area of overlap between two curves: $K(s)$ and $\dot{x}(t-s) - \dot{y}(t-s)$. In this sense $K(t)$ is subtly different from the control input used in a standard optimal control problem (as discussed in Chapter 3). The objective function of the system is defined by the area under the position, $x(t)$, curve. The states of the system are identified as the position and velocity of the mass m. $[x, \dot{x}]^T = [\xi_1, \xi_2]^T$. The optimal control problem

is formulated as follows:

$$\begin{aligned} &\underset{\mathbf{x}}{\text{minimize}} \int_{t_0}^{t_f} |\xi_1| \\ &\text{subject to} \\ &\qquad \dot{\boldsymbol{\xi}} = \mathbf{f_d}(\boldsymbol{\xi}(t), K(t), t), \\ &\qquad \boldsymbol{\phi}(t_0, \boldsymbol{\xi}(t_0)) = \mathbf{0} \end{aligned} \tag{5.1}$$

where,

$$\dot{\boldsymbol{\xi}} = \begin{bmatrix} \dot{\xi}_1 \\ \dot{\xi}_2 \end{bmatrix} = \begin{bmatrix} \xi_2 \\ -\frac{k}{m}(\xi_1 - y) - \frac{1}{m}\int_{t_0}^{t_f} K(s)\left(\xi_2(t-s) - \dot{y}(t-s)\right) ds \end{bmatrix} \tag{5.2}$$

$$\tag{5.3}$$

$\boldsymbol{\phi}(\cdot)$ represents the boundary constraints on the the states and the initial state of m is at rest and considered to be $\mathbf{0}$. The objective function is the area under the position trajectory of the mass m. $\mathbf{x}$ represents the optimization variable, that can be the state $\boldsymbol{\xi}(t)$, control $K(t)$, initial time, t_0 , final time , t_f or a combination of any two or more of these variables i.e., $\mathbf{x} = [\boldsymbol{\xi}(t),\ K(t),\ t_0,\ t_f]^{\mathrm{T}}$.

As discussed in Chapter 3, two methods of direct optimal control - namely, single shooting and direct transcription are applied to the vibration isolator case study problem. In this case, $K(t)$ is considered as the independent control input and the objective is to design an optimal trajectory of $K(t)$ so as to minimize the vibration of the mass m. Fig. 5.1 elaborates the application of the two methods to our case study.

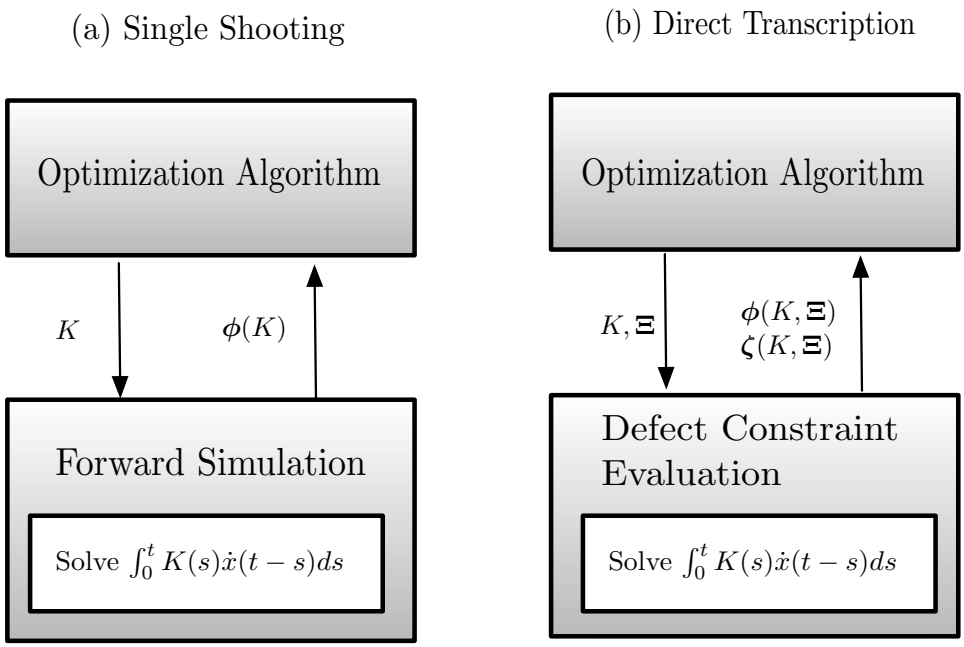

Figure 5.1: The two direct optimal control methods applied to the viscoelastic design problem. The relaxation modulus $K(t)$ is treated as the control input. (a) Single shooting involves a nested simulation of the dynamic system and is an example of a sequential approach. (b) Direct Transcription is a simultaneous approach that requires the evaluation of the dynamic equations as defect constraints and solves a large nonlinear program.

5.1.1 Convolution Sum

Before we demonstrate each of these approaches, it is important to understand one other key feature of the time-marching process — solving the convolution integro-differential equation. For this purpose a convolution sum is utilized. The value of the convolution integral at discrete points in time is denoted $\mathbf{I} = [I_1, I_2, \ldots, I_{n_t}]^{\mathrm{T}}$, where I_k is the value of the convolution integral at t_k. Here this is evaluated using a convolution sum:

$$I_k = \sum_{j=0}^{k} K(j)(\xi_2(k-j+1) - \dot{y}(k-j+1)) \tag{5.4}$$

$$\mathbf{I} = \int_0^t K(s)\left(\xi_2(t-s) - \dot{y}(t-s)\right) ds \tag{5.5}$$

In order to validate this discretization, a test was performed on the convolution of two simple functions whose analytical solution was known.

$$f(t) = e^{-t} \tag{5.6}$$

$$g(t) = \sin(t) \tag{5.7}$$

The analytical solution for the convolution is given by:

$$f * g = \int_0^t f(\tau)g(t-\tau)d\tau = \frac{1}{2}(e^{-t} + \sin t - \cos t) \tag{5.8}$$

The solution obtained from both the closed form solution and the convolution sum approach are shown in Fig. 5.2. Having validated the convolution

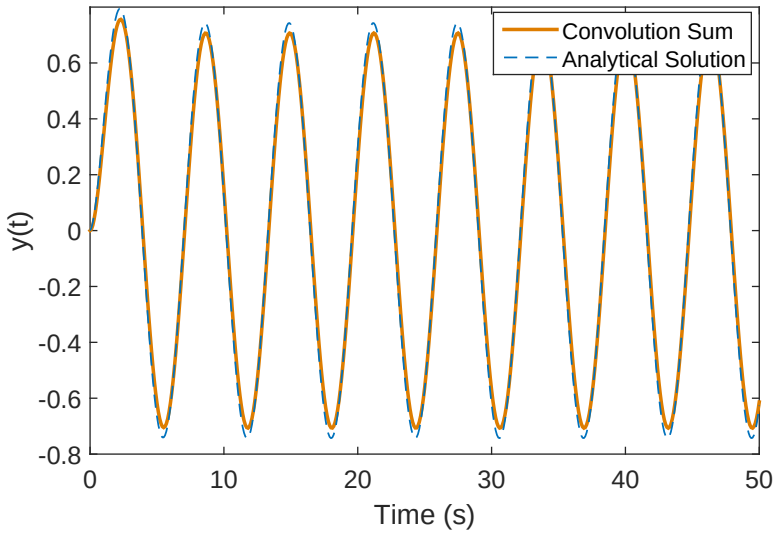

Figure 5.2: The results of the convolution of $f * g = \int_0^t e^{-\tau} \sin(t-\tau)d\tau$ are shown. We can see that the convolution sum gives almost exactly the same function value as the closed form solution.

sum methodology, we move onto integrating this with an optimal control approach.

5.2 A single shooting approach

As the initial step to implementing generalized viscoelastic design, we use the single shooting class of direct optimal control methods. In this method, the state space system is simulated forward in time using Forward Euler as the

time-marching scheme. The Forward Euler scheme is a simple time-marching method, in which the states are marched forward in time, given an initial set of conditions.

Assuming we discretize our time into n_t time steps starting from t_0 i.e., $t_0 < t_1 < \ldots < t_f$ and t_k represents the k time step and $h_k = t_k - t_{k-1}$, the Forward Euler method is given by:

$$\boldsymbol{\xi}[t_k] = \boldsymbol{\xi}[t_{k-1}] + h_k \mathbf{f_d}(\boldsymbol{\xi}[t_{k-1}], K[t_{k-1}], t_{k-1}) \tag{5.9}$$

While Eqn. (5.9) is the general representation of using Forward Euler with single shooting, the viscoelastic problem at hand is different in its dependence on previous time steps. As expressed in Eqn. (5.4), the existence of the convolution integral implies that the integrand (in this case, $K(t)$ and $\xi_2(t) - \dot{y}(t)$) depends on all previous states in time. The simulation for our system becomes subtly different in expression and vastly different in computation and can be represented as:

$$\boldsymbol{\xi}[t_k] = \boldsymbol{\xi}[t_{k-1}] + h_k \mathbf{f_d}(\boldsymbol{\xi}[t_0 : t_{k-1}], K[t_0 : t_{k-1}], [t_0 : t_{k-1}]) \tag{5.10}$$

where $[t_0 : t_{k-1}]$ represents the time from t_0 up until the time step t_{k-1}.

Prior to the application of single shooting, simulating the system with no control input i.e., without the existence of $K(t)$, we can see from Fig. 5.3 that the system exhibits unstable dynamics. The aim of introducing $K(t)$ is to stabilize the system and to minimize the amplitude of vibration. The single shooting algorithm aims to find an optimal $K(t)$ that achieves this objective.

The case study presented here has not been solved in the past using an optimal control approach. Hence, it involved an incremental development process. An initial formulation involved no constraints on the control, $K(t)$. The constraint on $dK(t)/dt$ was later added to ensure a time-decaying $K(t)$, which is a typical characteristic reported in literature for passive materials [20, 21]. The optimal control problem for the single shooting approach is

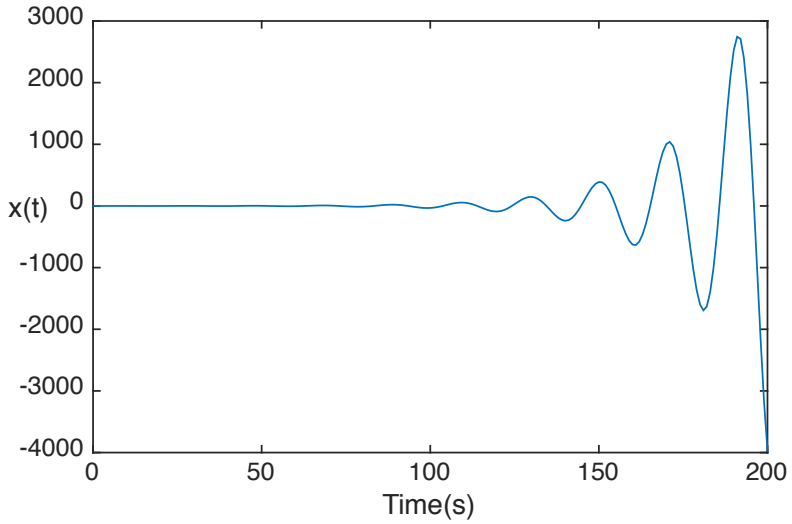

Figure 5.3: Unstable dynamics demonstrated by the vibration isolator system without the presence of a viscoelastic element. The plot represents the position of mass m over time.

formulated as follows:

$$\begin{aligned} \min_{\mathbf{K}} \quad & \int_{t_0}^{t_f} |\xi_1| \\ \text{subject to} \quad & \boldsymbol{\xi}(t_0) = \mathbf{0} \\ & \frac{dK(t)}{dt} \leq 0 \end{aligned} \tag{5.11}$$

where $\dot{\boldsymbol{\xi}} = \mathbf{f_d}(\boldsymbol{\xi}(t), K(t), t)$ is satisfied via simulation, and the time derivative function is defined as:

$$\mathbf{f_d}(\cdot) = \begin{bmatrix} \xi_2 \\ -\frac{k}{m}(\xi_1 - y) - \frac{1}{m}\int_{t_0}^{t_f} K(s)\left(\xi_2(t-s) - \dot{y}(t-s)\right) ds \end{bmatrix}$$

In this case $K(t)$, is parameterized at uniformly discretized points in time: $\mathbf{K} = [K(t_1), K(t_2), \ldots, K(t_{n_t})]^{\mathrm{T}}$, and the optimization is performed with respect to these n_t discrete values. As a result the derivative constraint is transformed into a set of linear algebraic inequality constraints.

5.3 Direct Transcription

In the DT formulation both the state and control trajectories are discretized in time. The overall size of the optimization problem is larger but the need for nested simulation is now eliminated and numerical behavior is improved. The OCSD problem for the DT implementation is formulated as:

$$\begin{aligned} \min_{\boldsymbol{\Xi},\mathbf{K}} \quad & \int_{t_0}^{t_f} |\xi_1| \\ \text{subject to} \quad & \boldsymbol{\xi}(t_0) = \mathbf{0} \\ & \frac{dK(t)}{dt} \leq 0 \\ & \boldsymbol{\zeta}(\boldsymbol{\Xi}(t), \mathbf{K}) = \mathbf{0} \end{aligned} \tag{5.12}$$

where $\boldsymbol{\Xi}$ is the matrix of discretized state trajectories (the ith row is the state vector values for time t_i), $\boldsymbol{\zeta}(\cdot)$ are the defect constraints. Trapezoidal quadrature was used to formulate both the defect constraints and to evaluate the objective function integral. For n_t discretized points in time, the objective function and defect constraints are:

$$\int_{t_0}^{t_f} |\xi_1| = \frac{1}{2} \sum_{k=1}^{n_t} h_k \left(|\xi_1[t_k]| + |\xi_1[t_{k-1}]| \right) \tag{5.13}$$

$$\boldsymbol{\zeta}[k] = \boldsymbol{\xi}[t_k] - \boldsymbol{\xi}[t_{k-1}] - \int_{t_0}^{t_f} \mathbf{f_d}(\boldsymbol{\xi}(t), K(t), t) = 0 \tag{5.14}$$

$$\boldsymbol{\zeta}[k] = \boldsymbol{\xi}[t_k] - \boldsymbol{\xi}[t_{k-1}] - \frac{h_k}{2} (\mathbf{f_d}[t_k] + \mathbf{f_d}[t_{k-1}]) = 0 \tag{5.15}$$

As in the single shooting case, since $K(t)$ is discretized at all points in time, the constraint on the derivative of $K(t)$ becomes a set of linear inequality constraints:

$$-K[t_k] + K[t_{k-1}] \leq 0 \tag{5.16}$$

In this preliminary implementation, the defect constraints are considered as non-linear design constraints and thus the convolution integral is still a part of the formulation. In a more involved DT implementation, the objective would be to exploit the problem structure and eliminate the need to integrate over previous states and control at every time step. The defect constraint

along with the convolution sum evaluation gives rise to the expression in Eqn. (5.17).

$$\boldsymbol{\zeta}[k] = \boldsymbol{\xi}[t_k] - \boldsymbol{\xi}[t_{k-1}] - \frac{h_k}{2}(\mathbf{f_d}[t_0 : t_k] + \mathbf{f_d}[t_0 : t_{k-1}]) = 0 \tag{5.17}$$

5.4 Results

On implementing both methods of optimal control, it is found that Direct Transcription achieves better attenuation of the vibration amplitude than with single shooting (as shown in Fig. 5.4), but requires more function evaluations to solve the discretized NLP. The number of function evaluations may not however be a fair comparison in this case as single shooting might involve nested derivative function calls. A logical next step would be to compare the total number of derivative function evaluations in both cases, in order to draw a better comparison. The objective function values and function evaluations are reported in Table 5.1. These results are also compared in Fig. 5.4 to the optimal design based on a Maxwell model parameterization (identified in Chapter 4). However it must be noted that the objective function used in the optimal control problem is different from the one used in Chapter 4. The comparison is used to demonstrate a similar behavior of both the Maxwell model and the state trajectory obtained from optimal control methods. The DT implementation here is a basic approach; several steps could be taken to take advantage of problem structure and improve efficiency, including polynomial representations of trajectories that reduce the number of time steps required and support closed-form integral solutions.

The optimal $K(t)$ trajectories are also shown in Fig. 5.5. These trajectories do not strictly fall into any of the parameterizations identified in Table 3.1. This is an exciting result that goes beyond what might be achieved using conventional material design methods. A physical realization of $K(t)$ could require one or many combinations of various sub-classes of materials that are available to a material designer today. This type of target function also presents an opportunity for significant innovation in material design with potential for impact on system performance. The optimal target provides new insights into what kind of functionality is needed to maximize overall system performance.

Table 5.1: The results from using DT and Single shooting are compared. While single shooting requires fewer function evaluations, direct transcription arrives at a better solution. The number of function evaluations cannot be taken at face value, as single shooting might involve nested derivative function evaluations, that are not included in the function calls returned by the optimization algorithm.

Method	**Objective Function value**	**F-Count**
Single Shooting	29.0786	8178
Direct Transcription	19.1916	78064

5.5 Conclusions

Materials used in engineering design are most often hard materials. Challenges associated with conceptual understanding and mathematical modeling of soft rheologically complex materials, such as viscoelastic materials, may be important factors in the limited use of soft materials in engineering design. The study on viscoelastic material design aims to improve this situation by connecting system-level design with generalized kernel targets that can then be used to guide material-level design. A more generalized treatment of $K(t)$ supports more complete and flexible design space exploration, and we postulate that it may help reduce design fixation and enhance design innovation.

Taking the example of linear viscoelastic systems, a systematic modeling procedure was laid out and the constitutive integro-differential equations were discussed in detail. The challenges in designing a generalized viscoelastic material with no a priori assumptions on its mathematical model were elaborated. Finally, the motivation to use direct optimal control in generalized viscoelastic design was presented. The application of direct optimal control was demonstrated by means of a vibration isolator problem. The findings show that adding a generalized viscoelastic element helps attenuate vibration, while allowing for design freedom. Of the direct optimal control methods used, direct transcription achieves a better performance than single shooting. Improvements in DT for IDEs could help reduce overall expense. While the resulting $K(t)$ target obtained does not fit into existing parame-

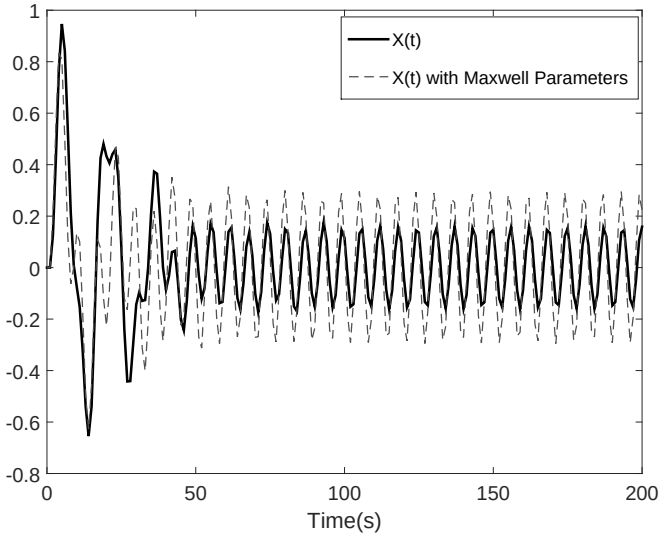

(a) The optimal trajectory of $x(t)$ from Single Shooting

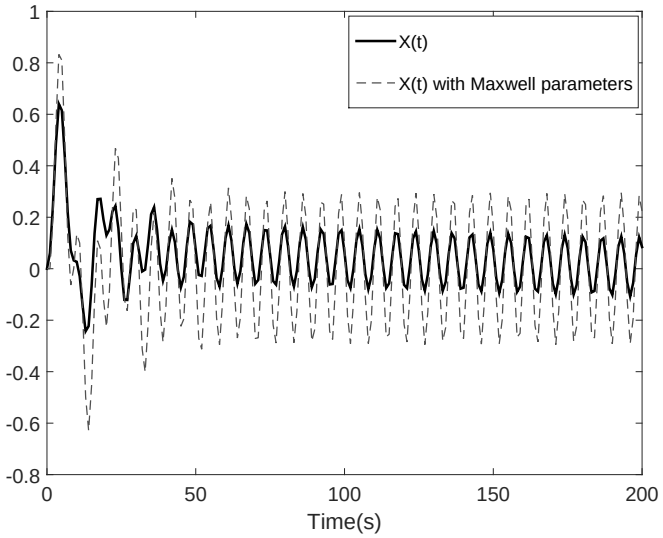

(b) The optimal trajectory of $x(t)$ from Direct Transcription

Figure 5.4: Results for optimizing the problem using (a) Single Shooting and (b) Direct Transcription. Direct Transcription achieves a better optimum than single shooting. The optimal amplitude trajectories are compared to the ones obtained using a Maxwell parameterization [27]. While it is an early stage design with a different objective function than in the previous chapter, the results are similar in nature to the Maxwell model. This might provide insights into obtaining a physically realizable $K(t)$.

terizations readily, it provides insights into the possibilities of using various classes to materials to achieve an optimal target.

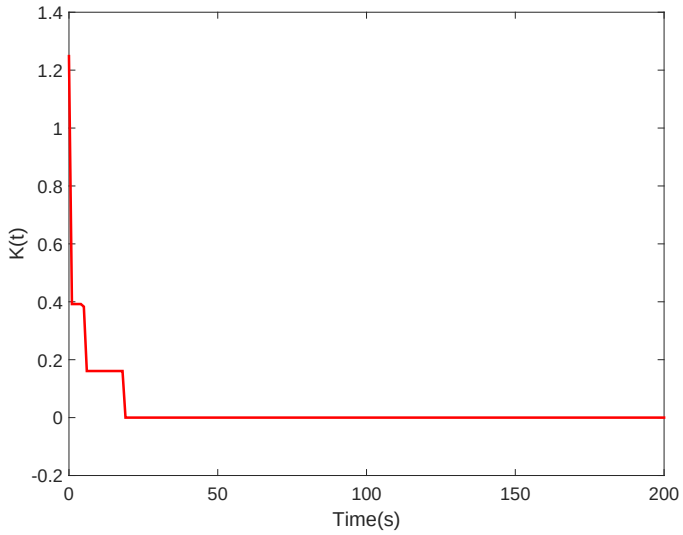

(a) Optimal $K(t)$ obtained from Single Shooting

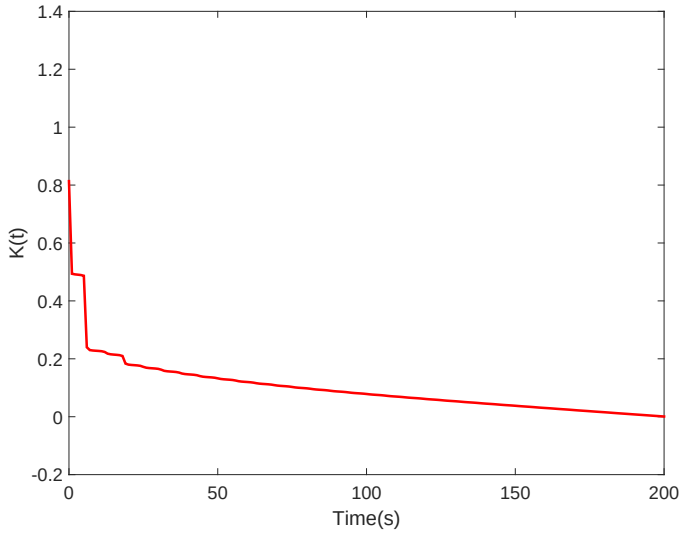

(b) Optimal $K(t)$ obtained from Direct Transcription

Figure 5.5: Optimal $K(t)$ trajectories are shown for (a) Single Shooting and (b) Direct Transcription. While these trajectories may not be directly physically realizable, they provide initial insights into modeling material classes that exhibit optimal target functions. Subsequent problem reformulations can help guide results toward physically realizable material behavior targets.

As a subsequent step, we identify using a state-space approximation of the convolution integral as another important strategy to investigate as a simultaneous approach to viscoelastic material design [57].

In this method the convolution integral (I) is approximated by using a linear sub-system. Let us consider:

$$\dot{\mathbf{X}}_p(t) = \mathbf{A}_p\mathbf{X}_p(t) + \mathbf{B}_p u_p(t) \tag{5.18}$$

$$I = y_p(t) = \mathbf{C}_p\mathbf{X}_p(t) \tag{5.19}$$

where $\mathbf{X}_p(t) = [x_1(t), x_2(t), x_3(t)]$ is the state vector of the linear sub-system. We can use any number of states, using as low as 3 states has been proved to be sufficient [57].

$$\mathbf{A}_p = \begin{bmatrix} 0 & 0 & -a_1 \\ 1 & 0 & -a_2 \\ 0 & 1 & -a_3 \end{bmatrix} \tag{5.20}$$

$$\mathbf{B}_p = [b_1 b_2 b_3]^T \tag{5.21}$$

$$\mathbf{C}_p = [0\ 0\ 1] \tag{5.22}$$

$$u_p(t) = \xi_2(t) - \dot{y}(t) \tag{5.23}$$

$$\tag{5.24}$$

We evaluate the coefficients of $\mathbf{A}_p$ and $\mathbf{B}_p$ by minimizing the following target function (using n_t time-steps).

$$Q = \sum_{k=1}^{n_t} G(t_k)[K(t_k) - \mathbf{C}_p e^{\mathbf{A}_p t_k}\mathbf{B}_p]^2 \tag{5.25}$$

where $G(\cdot)$ represents a weighting function, whose value is known at all the n_t time steps.

Modifying the constitutive equation of the vibration isolator problem by substituting $z = x - y$, we get:

$$-kz - \int_{t_0}^{t_f} K(s)\dot{z}(t-s) - m\ddot{z} = m\ddot{y} \tag{5.26}$$

Incorporating the state space approximation into the system dynamic equation leads to the following overall system state space model.

$$\mathbf{X}(t) = [x_1(t)\ x_2(t)\ x_3(t)\ z(t)\ \dot{z}(t)]^{\mathrm{T}} \tag{5.27}$$

$$u_f(t) = m\ddot{y}(t) \tag{5.28}$$

The state space matrices are given by:

$$\mathbf{A} = \begin{bmatrix} 0 & 0 & -a_1 & 0 & b_1 \\ 1 & 0 & -a_2 & 0 & b_2 \\ 0 & 1 & -a_3 & 0 & b_3 \\ 0 & 0 & 0 & 0 & 1 \\ 0 & 0 & -1/m & -k/m & 0 \end{bmatrix} \tag{5.29}$$

$$\mathbf{B} = [0\ 0\ 0\ 0\ -1/m] \tag{5.30}$$

$$\mathbf{C} = [0\ 0\ 0\ 1\ 0]^{\mathrm{T}} \tag{5.31}$$

Thus, the simultaneous formulation can be expressed as:

$$\begin{aligned} \min_{\boldsymbol{\Xi},\mathbf{K},\mathbf{A}_p,\mathbf{B}_p} \quad & \int_{t_0}^{t_f} |z| \\ \text{subject to} \quad & \mathbf{X}(t_0) = \mathbf{0} \\ & \frac{dK(t)}{dt} \leq 0 \\ & \boldsymbol{\zeta}(\mathbf{X}(t), \mathbf{K}) = \mathbf{0} \\ & Q = \sum_{k=1}^{n_t} G(t_k)[K(t_k) - \mathbf{C}_p e^{\mathbf{A}_p t_k} \mathbf{B}_p]^2 \leq \epsilon \end{aligned} \tag{5.32}$$

where $\boldsymbol{\zeta}(\mathbf{X}(t), \mathbf{K}) = \dot{\mathbf{X}}(t) - \mathbf{A}\mathbf{X}(t) - \mathbf{B}u_f$ and ϵ is a chosen tolerance value.

Cumulatively, a benchmarking of the the numerical methods with respect to efficiency and convergence would be required. The other crucial part in our future exploration is to understand the physical realizations of the optimal target $K(t)$. By understanding the relationship between the target and physically feasible materials, we can potentially go on to create a better mathematical model of a generalized viscoelastic system.

CHAPTER 6

Adaptive Surrogate Modeling based Multi-Objective Optimization

Many engineering applications involve multiple design objectives, typically centered on enhancing performance and reducing cost. Apart from having multiple design goals, engineering systems are also usually characterized by computationally intensive simulations. Despite advances in computing power in the recent past, computationally intensive analysis methods (e.g., Computational Fluid Dynamics (CFD)) can be impractical to use with optimization directly [2]. Important fluid power system design objectives, such as friction across sliding contacts, often require an expensive CFD simulation of the Navier-Stokes equation for each new design candidate. One effective strategy for reducing the total number of high-fidelity simulations required to solve a design optimization problem is optimize using an approximate surrogate model (SM)—sometimes called a *meta-model*—of the high-fidelity model [64, 65]. Accurate solution requires acceptable SM accuracy in the neighborhood of the optimum. Adaptive surrogate modeling methods iteratively assess SM accuracy, and evaluate the high-fidelity model at new sample points to improve SM accuracy if needed in strategic regions of the design space [66, 67]. The cost of evaluating sample points using the high-fidelity model must be accounted for when comparing SM to direct optimization.

SM has been investigated for specific application domains, such as structural design [68] and injection molding [69]. While most studies have focused on single-objective problems (e.g., Ref. [70]), extensions of SM to MOO have been made [69]. This chapter presents advancements of adaptive SM for MOO that aim to reduce the number of required simulations further. New features of this method include enforcement of constraints during high-fidelity model sampling. The algorithmic approach is elucidated using a mathematical example, followed by a physical engineering application that employs a CFD simulation of Newtonian fluids on microtextures.

6.1 Adaptive SM Methodology

In this section the adaptive surrogate modeling (ASM) method is explained in detail, including steps for formulating the multi-objective optimization problem and implementing the adaptive strategy for incrementally improving surrogate model accuracy in strategic design space regions.

6.1.1 MOO Problem Formulation

Formulating an underlying engineering design problem as a mathematical optimization problem involves identifying design objectives, variables, and constraints based on a firm understanding of the physical system and design requirements and intent. A multi-objective optimization problem can be formulated as follows:

$$\begin{aligned} \min_{\mathbf{x}=[x_1,x_2,\ldots,x_n]^{\mathrm{T}}} \quad & \mathbf{f}(\mathbf{x}) = [f_1(\mathbf{x}), \ldots, f_m(\mathbf{x})]^{\mathrm{T}}, \\ \text{subject to} \quad & \mathbf{g}(\mathbf{x}) = [g_1(\mathbf{x}), \ldots, g_p(\mathbf{x})]^{\mathrm{T}} \leq \mathbf{0} \\ & \mathbf{h}(\mathbf{x}) = [h_1(\mathbf{x}), \ldots, h_q(\mathbf{x})]^{\mathrm{T}} = \mathbf{0} \\ & \mathbf{x}_{LB} \leq \mathbf{x} \leq \mathbf{x}_{UB} \end{aligned} \tag{6.1}$$

where $\mathbf{f}(\mathbf{x})$ is a vector-valued objective function, $\mathbf{x}$ is the vector of design variables, $\mathbf{g}(\cdot)$ and $\mathbf{h}(\cdot)$ are constraint functions, and $\mathbf{x}_{LB}$ and $\mathbf{x}_{UB}$ are design variable bounds.

6.1.2 SM-Based Multi-Objective Optimization

The next step in solving Prob. (6.1) using a surrogate modeling strategy is to construct a model based on *training data*, i.e., a set of design points and the corresponding objective and constraint function values based on high-fidelity simulation. The SM is computationally inexpensive, allowing many function evaluations required for identifying an optimal design. The resulting design solution is only optimal with respect to the SM, so SM accuracy at the predicted optimum must be assessed by checking high-fidelity model outputs at this point. One of three strategies typically are used for ensuring accurate solution (Fig. 6.1).

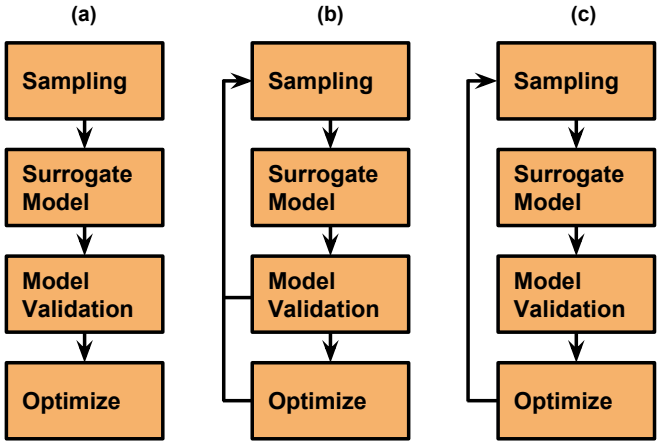

Figure 6.1: Strategies for SM-based design optimization: (a) Sequential, (b) Adaptive, (c) Direct Sampling [64]

The first (Fig. 6.1(a)) is a sequential approach with a single validation check after SM construction but before optimization. This requires error assessment across the entire modeling domain to ensure accurate solution, involving a large number of validation points that must be evaluated using the high-fidelity model. Sequential sampling methods that treat the model development and optimization as independent tasks. Efficiency can be improved by adopting an iterative method where additional training data is obtained via additional sampling to improve SM accuracy if model validation fails (Fig. 6.1(b)). Wang et al. studied adaptive sampling as a means to improve a surrogate model prior to (single objective) optimization [71]. In this case, both the optimization and model validation points (a more global approach) are used to form a new sample set. High-fidelity model evaluations can be reduced further by using a direct sampling approach where new sample points are concentrated near the optimum predicted via SM optimization (Fig. 6.1(c)).

Additional challenges are introduced for MOO problems. Instead of needing to ensure SM accuracy in the neighborhood of a single predicted optimal point, the SM must be accurate in the neighborhood of the set of Pareto-optimal designs. Wilson et al. introduced an approach that ensured model validation and accuracy prior to identifying the Pareto-set [72]. Li et al. ap-

proximated Pareto sets using a hyper-ellipse [73]. Shan and Wang developed a new method—Pareto-Set Pursuing (PSP)—that addresses the challenges of solving MOO problems based on computationally expensive models [74].

The Adaptive Surrogate Modeling method for Multi-Objective Optimization (ASM-MOO) methodology presented here is a direct sampling approach. The case study involves a challenging fluid-flow system design problem, but the methodology can be extended to a general class of design problems. We introduce design constraint enforcement at the sampling stage, and study the resulting efficiency of this modified sampling method.

6.2 ASM-MOO Algorithm Framework

A more detailed illustration of the ASM-MOO methodology is shown in Fig. 6.2. The modeling domain D_m is the region of the design space over which the SM is constructed. This may be fixed, or may contract and shift to conserve modeling efforts. The superscript k is the iteration counter. The sampling domain D_s is the design space region over which new sample points are defined; design sample points and their corresponding simulation outputs are used for the training dataset T.

During initialization the sampling domain D_s is defined to be the same as the modeling domain, as no information is available yet to help focus sampling efforts near the predicted Pareto-optimal points. It is desirable to avoid using sample points that violate design constraints for two reasons: 1) Often infeasible points cannot be simulated [75], and 2) even if simulation is possible, simulation of infeasible points is wasted effort as SM accuracy is unimportant in infeasible regions. Here a set of preliminary samples are generated using one of several appropriate space-filling sampling techniques (such as Latin Hypercube) in the preliminary sampling domain $\tilde{D}_s$. This domain may include infeasible points. This set of sample points is then filtered to remove infeasible points, i.e., retained sample points belong to the set $D_s = \tilde{D}_s \in F$, where F is the feasible domain (i.e., the set of points that satisfy design constraints). In the studies presented here design constraints are analytical, so SMs for design constraints are not needed.

T is then formed by evaluating each retained sample point using the high-fidelity model, and organizing these data pairs. The SM is then constructed

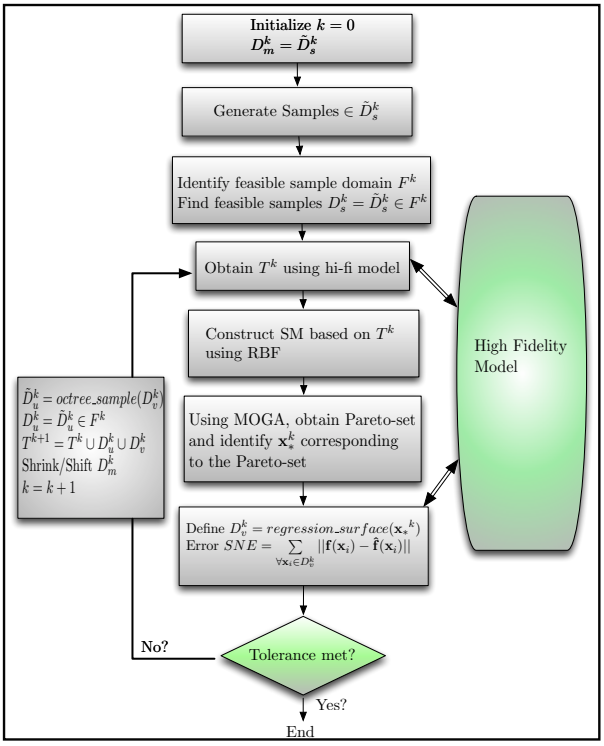

D_m	Modeling domain
$\tilde{D}_s$	Initial Sampling domain
F	Feasible domain
D_s	Feasible Sampling domain
T	Training Dataset
$\mathbf{x}_*$	Optimal design variable
D_v	Validation domain
$\tilde{D}_u$	Updated Sampling domain
D_u	Updated Feasible Sampling domain

Figure 6.2: ASM-MOO algorithm

using T. Here radial basis functions are used to create the model [76]. The MOO problem is then solved using an appropriate algorithm (MOGA here) and function evaluations based on the SM to obtain a set of approximately Pareto-optimal points $\mathbf{x}_*$.

Model validation is performed by assessing SM error at points in the Pareto set (analogous to assessing SM error at the predicted optimum for single-objective problems). If the selected error metric does not satisfy a specified error tolerance, the process is repeated by generating new sample points near the current Pareto set, running the high-fidelity model at these new points, and adding these points to T. A new (more accurate) SM is formed, and optimization is repeated. Additional details for these steps are presented below [77].

6.2.1 Sampling

The modeling domain $\tilde{D}_m$ is defined here by the design variable bounds. Due to the SM type and the nature of the case studies, $\tilde{D}_m$ was not adjusted during the the ASM-MOO process. Here $\tilde{D}_s = D_m$, and a suitable design of experiments (DOE) technique is used to generate sample points that lie in $\tilde{D}_s$. The appropriate choice of sampling technique depend on factors such as (i) design space dimension, (ii) estimated level of response noise, and (iii) SM type. For noisy data (e.g., probabilistic models), DOEs that reduce the sensitivity to noise are desirable, such as central composite designs, face-centered cubic designs, factorial designs, and Box-Behnken designs [78]. For systems with less noise (such as deterministic models), Latin-Hypercube Sampling (LHS), minimum bias designs, and Orthogonal Arrays (OAs) are preferred. Here LHS is used, which is an example of a *space-filling* design that is often effective for computer experiments without variance [79–81], including adaptive surrogate modeling [82] and in conjunction with OAs [83].

6.2.2 Filtering Infeasible Sampling Points

Engineering design problems often involve inequality constraints $\mathbf{g}(\cdot) \leq \mathbf{0}$. The sampling procedure described above ensures that only feasible design points are evaluated using the high-fidelity model, improving overall efficiency. In some cases this strategy offers another important advantage: sample points that violate constraints may not be physically meaningful, or for other reasons would cause simulation failure. Removing infeasible preemptively avoids these simulation problems that are otherwise difficult to manage in an optimization implementation [75]. We investigate how filtering out infeasible sample points influences solution efficiency.

While this algorithm addresses only analytically defined linear and nonlinear constraints, we acknowledge the need to extend this study to constraints that require the simulation of the high-fidelity model. Filtering out infeasible points based on approximated constraint functions is an important topic for future work. It is expected that additional challenges will be encountered as there is uncertainty in whether sample points are actually infeasible during the ASM solution process.

6.2.3 Surrogate Model Construction

Once the set of feasible sample points is defined, these design points are evaluated using the high-fidelity model. This produces input-output pairs that are added to the set of training data T to be used for SM construction. A wide variety of approximation function types may be used for SM construction. Several general-purpose options are described below. Application-specific SMs may help improve solution efficiency further.

General purpose approximation functions for SMs help to estimate simulation output at design points other than those in T. Well-known options include Kriging [81, 84], artificial neural networks (ANNs) [85], and radial basis functions [86, 87]. Other methods include multivariate adaptive regression splines (MARS) [88], least interpolating polynomials [89], and inductive learning [90]. Jin et al. compared several different surrogate models and concluded that the appropriate model choice depends on the degree of system nonlinearity [91]. Stander et al. compared polynomial response surface approximation, Kriging, and neural networks [92], and discovered that while neural networks and Kriging models require a larger number of initial points, their algorithmic efficiencies are comparable to a polynomial model. The general conclusion from the literature demonstrates that there is no single best SM type that satisfies all problems. Haftka et al. address this issue by exploring the use of an ensemble or a weighted average SM in place of individual surrogates [93]. The best model choice depends on the nature of the problem and the sampled data set.

Radial basis functions have been used extensively as SMs for engineering design optimization [76, 94]. Fang et al. compared polynomial response and radial basis functions and found that RBFs are more effective at handling non-linearities in some cases [95]. RBF models have been selected for use in this article. Comparison with other model types is an important topic for future work.

When using an RBF approximation for multi-objective problems, an approximate function is defined for each of the m objective function values. As part of this definition, the interpolation condition for the jth objective function is formulated using n_s training points:

$$f_j(\mathbf{x}_i) = \sum_{k=1}^{n_s} w_k^j \psi(||\mathbf{x}_i - \mathbf{c}_k||), \quad i = 1, 2 \dots n_s \qquad j = 1, 2 \dots m \tag{6.2}$$

where $\psi(.)$ is the radial basis function, w_k^j are unknown weighting coefficients, $\mathbf{x}_i$ is the ith training point, and $\mathbf{c}_k$ is the kth basis function center. The RBF used here is the thin plate spline function [96]: $\psi(r) = r^2 \ln r$, where r is the Euclidean distance between the training point and function center: $r = (||\mathbf{x}_i - \mathbf{c}_k||)$.

During SM construction we seek to find the coefficients w_i^j that solve $\boldsymbol{\psi}\mathbf{w}^j = \mathbf{f}_j$, where $\psi_{i,k} = \psi(||\mathbf{x}_i - \mathbf{c}_k||)$, $i, k = 1, 2 \dots n_s$ is the Gram matrix, and the vector of training outputs for the jth objective function is $\mathbf{f}_j = [f_j(\mathbf{x}_1), f_j(\mathbf{x}_2), \dots, f_j(\mathbf{x}_{n_s})]^{\mathrm{T}}$ [96]. This equation has a unique solution since the Gram matrix is square. To reduce problem complexity here we assume that the RBF centers coincide with training points, i.e., $\mathbf{c}_i = \mathbf{x}_i$. Once the coefficients w_k^j are identified for each objective function the approximate objective functions can be defined: $\hat{\mathbf{f}}(\mathbf{x}) = [\hat{f}_1(\mathbf{x}), \dots, \hat{f}_m(\mathbf{x})]^{\mathrm{T}}$. For a given point in the design space $\mathbf{x}$, we can compute the row vector $\hat{\boldsymbol{\psi}}(\mathbf{x}) = [\psi(||\mathbf{x} - \mathbf{c}_1||), \dots, \psi(||\mathbf{x} - \mathbf{c}_{n_s}||)]$. The surrogate model for the jth objective function is $\hat{f}_j(\mathbf{x}) = \hat{\boldsymbol{\psi}}(\mathbf{x})\mathbf{w}^j$.

6.2.4 Surrogate Model Optimization

The multi-objective design optimization problem is then solved by replacing the original nonlinear functions in Prob. (6.1) with approximate functions obtained via surrogate modeling. This produces an approximate Pareto set that is only accepted as the solution if the validation step is passed. If all objective and constraint functions are approximated using surrogates, the updated problem formulation is:

$$\begin{aligned} \min_{\mathbf{x}=[x_1,x_2,\dots,x_n]^{\mathrm{T}}} \quad & \hat{\mathbf{f}}(\mathbf{x}) = [\hat{f}_1(\mathbf{x}), \dots, \hat{f}_m(\mathbf{x})]^{\mathrm{T}}, \\ \text{subject to} \quad & \hat{\mathbf{g}}(\mathbf{x}) = [\hat{g}_1(\mathbf{x}), \dots, \hat{g}_p(\mathbf{x})]^{\mathrm{T}} \leq \mathbf{0} \\ & \hat{\mathbf{h}}(\mathbf{x}) = [\hat{h}_1(\mathbf{x}), \dots, \hat{h}_q(\mathbf{x})]^{\mathrm{T}} = \mathbf{0} \\ & \mathbf{x}_{LB} \leq \mathbf{x} \leq \mathbf{x}_{UB} \end{aligned} \tag{6.3}$$

The solution of a MOO problem involves a set of solutions, known as the Pareto-optimal set (or Pareto set), that consists of non-dominated optimal points and quantifies design trade-offs in the objective function space. Many strategies exist for addressing MOO design problems [97, 98], some of which include condensing the multiple objectives into a single objective function by using a weighted sum or a geometric mean. An alternative treats all but one objective as a constraint. In either case multiple optimization solutions are required to build up the Pareto set, each time varying objective weights or constraint bounds. Another class of MOO solution methods are evolutionary algorithms such as the Multi-Objective Genetic Algorithm (MOGA) and the Non-dominated Sorting Genetic Algorithm (NSGA-II) [99, 100], both of which produce multiple Pareto-optimal solutions in a single optimization execution.

This MOO problem was solved here using a Multi-Objective Genetic Algorithm (MOGA), a specific class of evolutionary algorithms [101]. The primary advantage of evolutionary algorithms for MOO is that an approximate Pareto set can be generated via a single MOGA solution.

6.2.5 Surrogate Model Validation

Surrogate models used in design optimization need to be accurate in the region of the optimum. Guaranteeing accuracy within a tolerance at other points in the design points is wasteful of resources. Validation is straightforward for single objective problems where SM accuracy must be verified near the single predicted optimal point. This can be accomplished by evaluating the high-fidelity model at the predicted optimum, and comparing the result to the SM output at this point. SM validation is more involved for MOO problems. We need to ensure that the SM is accurate for points in the design space that are Pareto-optimal. Instead of validating the SM at a single point, it must be validated across a bounded hypersurface. For this purpose we define the validation domain D_v to be the set of points over which the SM must be validated. If the design space is in $\mathbb{R}^n$, the hypersurface that defines D_v is a manifold of dimension $n-1$.

Validating over bounded hypersurface introduces two core challenges: 1) Instead of validating a single point in the design space, validation must be

performed across an infinite number of points on a hypersurface, and 2) The boundaries of this hypersurface may be complicated (possibly non-convex or even disconnected), and we should focus validation efforts on points within the hypersurface bounds. The first challenge is addressed by using regression to fit a surface through Pareto-optimal points in the design space to define an approximate (unbounded) validation domain. A uniform sampling technique is then used to select a finite set of *validation points* from D_v for validation. Generating these new validation points in D_v is required because simply using the Pareto-optimal points identified by the MOGA as validation points may not be adequate due to non-uniform distribution in the design space. The error between the SM and the high-fidelity model is evaluated at these validation points, and these error quantities are combined into a single error metric for SM validation.

In addressing the second challenge we recognize that not every point on an unbounded regression surface that is fit through Pareto-optimal points is in the Pareto set. We must identify and stay within hypersurface bounds to ensure that validation points are (approximately) in the Pareto set.

Several options exist for defining the validation hypersurface D_v, including simple regression, non-uniform rational basis splines (NURBS) [102], or T-splines. Quadratic regression performed well for the small-dimension case studies used here. Support Vector Data Description (SVDD) could be used to define a precise hypersurface boundary that includes all known Pareto-optimal points [75, 103]. Rather than defining a precise boundary, we developed an algorithm that generated random points on the hypersurface that were within a convex hull of a subset of the known Pareto-optimal points. This provided an efficient means of generating validation points that were approximately in the true D_v.

Once validation points are chosen, the high-fidelity model is evaluated at these points for comparison to the SM to evaluate accuracy. Several options for SM validation exist, but standard methods are intended primarily for cases where accuracy is being assessed across D_m. Cross-validation is a popular method used for this purpose. It involves starting with a dataset, X, Y consisting of n input-output data pairs (x, y), where y is the high-fidelity model response at the design sample point, x, and n_s is the total number of function evaluations used for combined training and validation. In p-fold cross validation, the initial validation data set is split into p different subsets.

The metamodel is then fit p times, each time leaving out one of the subsets from training, and using the omitted subset for validation. Since this is computationally cumbersome, Meckesheimer [104, 105] suggested a leave-one out cross-validation strategy, applicable to radial basis functions.

The method used here is to evaluate the standard normal error (SNE) using points in D_v. For a set of n_v validation points, the norm of the difference between the actual function value and the approximated function value is defined as the SNE:

$$\text{SNE} = \sum_{i=1}^{n_v} ||(\mathbf{f}(\mathbf{x}_i) - \hat{\mathbf{f}}(\mathbf{x}_i))|| \tag{6.4}$$

where $\mathbf{x}_i$ is the design vector value for the ith validation point.

6.2.6 Sampling Domain Update

If the SNE $\geq \epsilon_v$, where ϵ_v is a specified validation tolerance, model accuracy must be improved in the neighborhood of the Pareto set. This is done by generating new sample points that are in $\tilde{D}_u$, which is the updated sampling domain that includes a small neighborhood of the design space near D_v. The high-fidelity model is evaluated at these new sample points, and these data pairs (along with the validation points from the previous set) are appended to T for use in constructing the updated SM with improved accuracy near the estimated Pareto set.

Sample points need to be defined that lie within $\tilde{D}_u$, which is a hypervolume. One approach would be to define the boundary of this hypervolume directly (using SVDD, level set methods, etc.) and filter out sample points that are not within this boundary. A classification method such as a Support Vector Machine (SVM) could be used to determine whether candidate sample points are within $\tilde{D}_u$ [103, 106]. Alternatively, force-directed layout or field functions could be used to increase the density of sample points near D_v.

The method used here is an Octree-based sampling method [107] that generates uniformly distributed points in the neighborhood of validation points as shown in Fig. 6.3. Sample point density can be adjusted as the ASM-MOO algorithm progresses. Given a specified distance tolerance, points lying far

from D_v are eliminated to produce $\tilde{D}_u$. In addition, only feasible sample points are retained. $D_u = \tilde{D}_u \in F$ defines the updated feasible sampling domain that contains new sample points to be simulated.

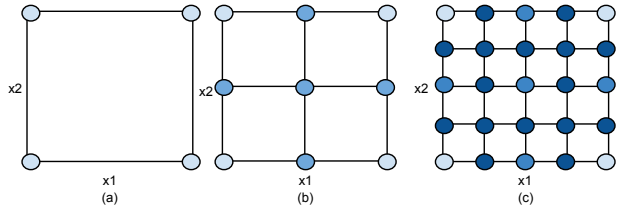

Figure 6.3: Octree-based sampling algorithm (two design variable example: x_1 and x_2). With an initial set of points to define the domain to sample from as shown in (a), the octree-based algorithm uniformly samples points within these bounds sparsely in (b) and more densely in (c) depending on sampling requirements.

Figure 6.4 illustrates conceptually the validation and sample point generation strategies described above using a two-dimensional design space. Yellow markers are MOGA Pareto-points. The solid black line is the validation domain D_v obtained via regression. Dark blue markers are the uniformly distributed validation points. The red curve is the design constraint boundary (up and to the right in infeasible). Red markers are new (infeasible) Octree sample points. Magenta markers are feasible sample points that are too far away from D_v to use. Cyan markers are the feasible sample points in D_u.

6.2.7 Modeling Domain Update

The modeling domain D_m can either remain static or can be contracted and re-centered to ease model construction. D_m contraction can be accompanied through a simple iterative formula: $\Delta_i^{k+1} = \beta\Delta_i^k$, where Δ_i^{k+1} is the range of x_i at the kth ASM-MOO iteration, and $\beta < 1$ is a fixed contraction parameter. One strategy for re-centering the modeling domain would be to align its center with the centroid of D_v. Rapid changes in D_m center may cause numerical instabilities, which could be ameliorated with numerical damping (e.g., the heavy ball method) [108]. Here D_m remains fixed as the update is performed close to the optimum. Variable bounds are determined by experimentally appropriate limits.

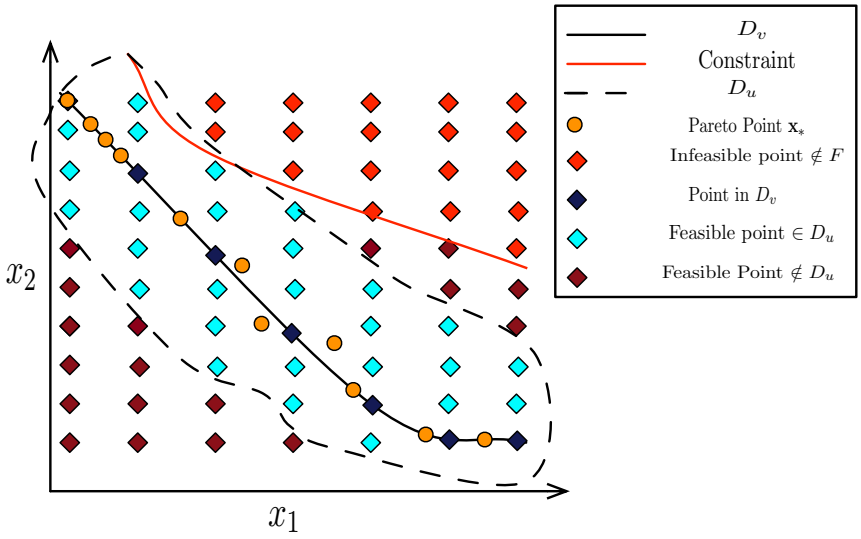

Figure 6.4: Conceptual illustration of validation point and sample point generation

6.2.8 Training Data Set Update

Before construction of the updated SM, the training data set is augmented with both the validation data and new sample points: $T^{k+1} = T^k \cup D_u^k \cup D_v^k$, where k denotes the kth iteration of the ASM-MOO algorithm.

Using the framework described in this chapter for adaptive surrogate modeling applied to multi-objective optimization problems, Chapter 7 will aim at implementing the algorithm on a mathematical problem followed by a hydraulic component design problem.

CHAPTER 7

Numerical Studies and Results using Adaptive Surrogate Modeling

The ASM-MOO algorithm is demonstrated first using a simple analytical multi-objective constrained optimization problem, and then using a more sophisticated case study involving design of efficient fluid power systems.

7.1 Analytical Example

Consider the following MOO problem:

$$\begin{aligned} \min_{\mathbf{x}=[x_1,x_2]^{\mathrm{T}}} \quad & \mathbf{f}(\mathbf{x}) = [f_1(\mathbf{x}), f_2(\mathbf{x})]^{\mathrm{T}}, \\ \text{where} \quad & f_1(\mathbf{x}) = (x_1-2)^2 + (x_2-1)^2 \\ & f_2(\mathbf{x}) = (x_1)^2 + (x_2-6)^2 \\ \text{subject to} \quad & -2.5x_1 + x_2 - 1 \leq 0 \\ & (x_2-2)^2 - 2 \leq 0 \\ & 0.4 \leq x_1 \leq 1.6, \quad 2 \leq x_2 \leq 5 \end{aligned} \tag{7.1}$$

This problem was solved in two ways: 1) using the MOGA algorithm available in MATLAB ® with direct objective function evaluation, and 2) using the ASM-MOO with the same MOGA algorithm. The result of the first solution approach is the baseline or 'true' solution. Both Pareto sets are shown in Fig. 7.1, and the error values are presented in Table 7.1.

If we allow the same number of total original function evaluations for the ASM-MOO method, using sample constraints to eliminate infeasible sample points results in slightly improved solution accuracy based on SNE. The total number of function evaluations was made approximately equal by increasing the number of initial sample points for the case with sample constraints. Additional benefits of sampling constraints may be realized with simulation-based problems (e.g., preventing simulation failure by avoiding infeasible

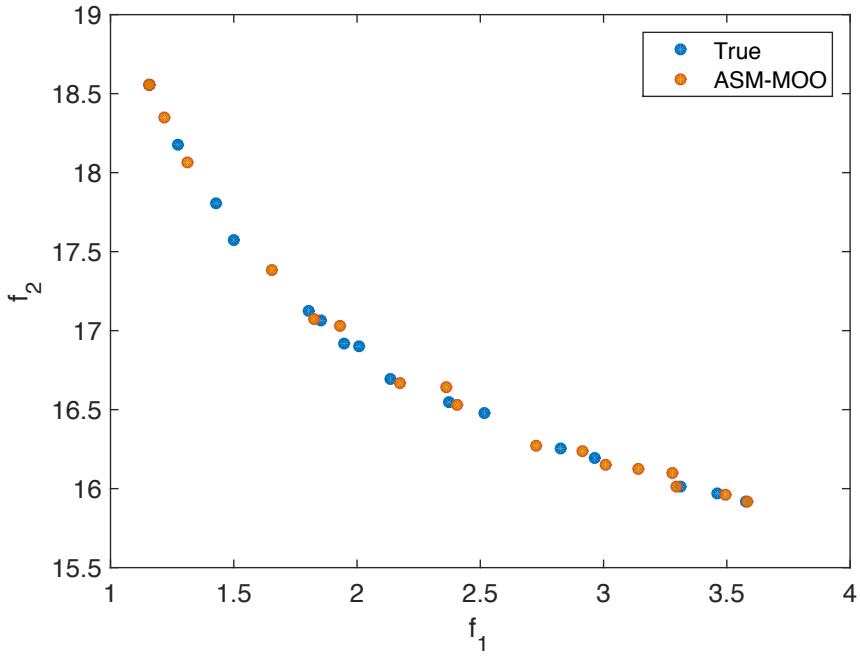

Figure 7.1: Comparison between Pareto sets obtained via direct optimization and via ASM-MOO

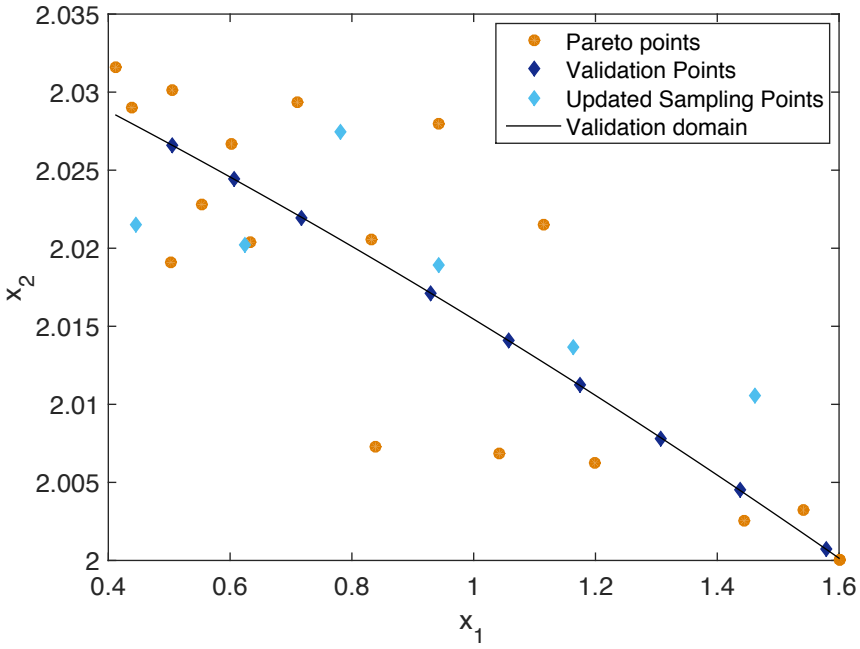

Figure 7.2: Pareto-values and the update domain in the design space.

designs).

Table 7.1: Results from using sampling constraints on the analytical example. In each case the methods used approximately the same number of original function evaluations.

Method	**No. of iterations**	**SNE**
ASM-MOO w/o sampling constraints	8	8.26e-04
ASM-MOO with sampling constraints	6	6.20e-04

7.2 Design for Efficient Fluid Power

A hydraulic system design study motivated the development of the ASM-MOO method introduced in this article. This study involves the investigation of different surface texture designs for components used in fluid power systems where metal parts are in sliding contact separated by hydraulic fluid. The competing design objectives investigated here include reducing effective viscosity (related to friction) and the cross-sectional area of the texture (related to cost).

Previous studies have shown that the use of surface textures aids in decreasing friction in lubricated sliding contact [109]. Schuh and Ewoldt [110] have experimentally examined the effects of using symmetric and asymmetric textures to decrease viscous friction and increase normal force production with Newtonian lubricants. For the experiments, a DHR-3 gap controlled rotational rheometer was used with the textured plates mounted to a temperature controlled Peltier plate with Crystalbond, a thermo-reversible adhesive. A schematic of the experimental set up is given in Fig. 7.3, and the measured geometric properties of the textures tested are given in Fig. **??**.

In their experiments, Schuh and Ewoldt found that symmetric textures decreased the viscous friction more than the asymmetric textures, but the asymmetric textures produced larger normal forces than the symmetric ones (important for sealing).

Since each texture profile met both of the given design objectives, but met them to differing degrees, this presents an interesting opportunity to study optimal tradeoffs for texture profile design. A computer experiment of the

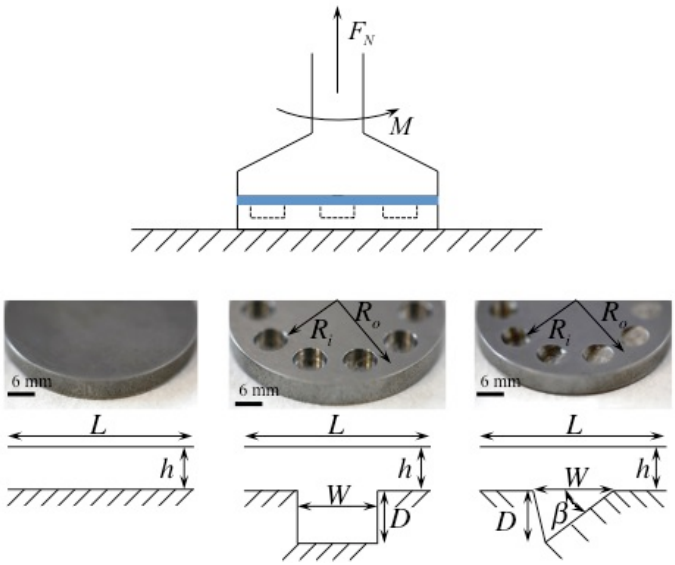

Figure 7.3: Experimental setup. Design variables are defined in Eqn. (7.2).

Table 7.2: Measured Geometric Parameters.

	Geometric Parameters		
	D[mm]	**W**[mm]	**L**[mm]
Flat Plate	–	–	–
Symmetric	2.28	6.0	8.953
$\beta = 21.7°$	2.04	5.88	8.953
$\beta = 14°$	1.5	5.98	8.953
$\beta = 9.4°$	1.03	6.0	8.953
$\beta = 5.3°$	0.5	6.0	8.953

physical setup provides a basis for evaluating texture design candidates. The simulation of the fluid-texture system requires a finite volume based CFD simulation, which is a computationally-expensive process, particularly when scaled to 3D. ASM-MOO was used to mitigate this expense. The MOO

problem for this case study is defined as follows:

$$\min_{\mathbf{x}=[x_1,x_2,x_3]^{\mathrm{T}}} \quad \mathbf{f}(\mathbf{x}) = [f_1(\mathbf{x}), f_2(\mathbf{x})]^{\mathrm{T}}, \tag{7.2a}$$

where

$$f_1 = \eta_a/\eta_0 \tag{7.2b}$$

$$f_2 = x_1 x_2 \tag{7.2c}$$

$$x_1 = \text{Texture width: W (mm)} \tag{7.2d}$$

$$x_2 = \text{Texture depth: D (mm)} \tag{7.2e}$$

$$x_3 = \text{Plate length: L (mm)} \tag{7.2f}$$

subject to

$$x_2 \leq 0.95 x_4, \tag{7.2g}$$

$$0 \leq x_1 \leq 6 \tag{7.2i}$$

$$0 \leq x_2 \leq 2 \tag{7.2j}$$

$$0.8953 \leq x_3 \leq 8.953 \tag{7.2k}$$

Training data was obtained via FLUENT, a finite volume-based CFD solver. Symmetric and asymmetric texture profiles were simulated at steady state in FLUENT using a Newtonian lubricant with a viscosity of 0.140 Pa s and a density of 866.8 kg/m^3. The simulations were performed using double precision and parallel computing with two processes. The pressure was solved using the SIMPLE algorithm and the momentum was solved using the second order upwind technique. A hybrid initialization scheme was used, and the simulation was run until all the residuals for the system were less than 1×10^{-5}. h was fixed at 0.25 mm. Several different values of W, D, and L were simulated in order to examine different texture profiles. The results from FLUENT were given as a normal force and viscous force, and the viscous force was converted to an apparent viscosity using:

$$\eta_a = \frac{F_v}{WL\frac{U}{h}} \tag{7.3}$$

where U is the velocity of the top plate, which for these simulations was set as $U = 1.425$m/s.

The design constraint $x_1 \leq 0.95 x_3$ ensures that texture width is no greater than 95% of the length of the moving plate. The simulation would be infeasible (or produce insensible output) if the constraint is violated. RBFs

were used as the surrogate model here. ASM-MOO was then applied to the design system to identify the optimal texture features. In this case, the validation domain D_v is a hypersurface as we have a 3-dimensional design space (Fig. 7.4).

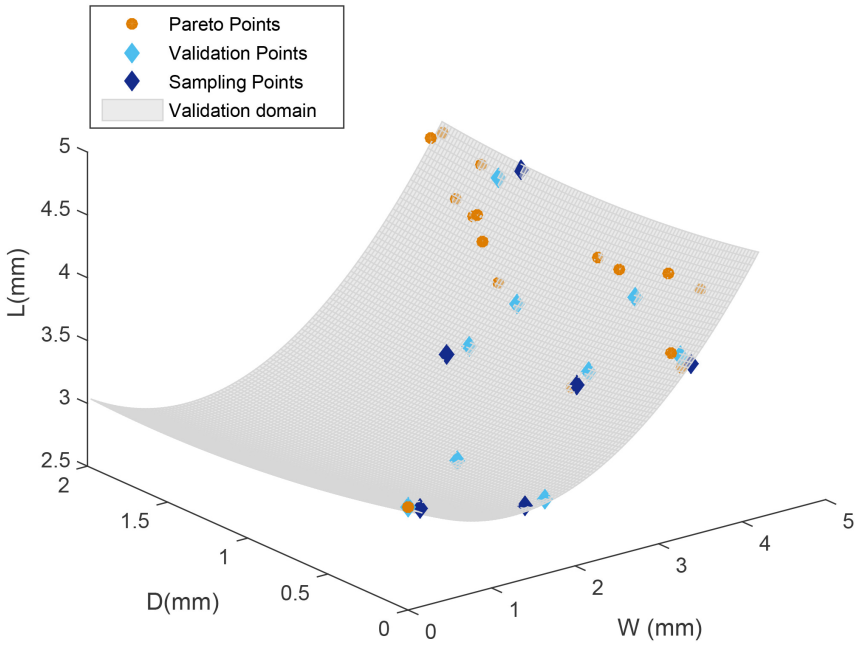

Figure 7.4: The Pareto-points, validation points, and updated sample points for the case study. The surface shown represents the validation domain, D_v.

Results presented here are preliminary and limited to the case of symmetric textures. The result is visualized as a Pareto set in Fig. 7.5. The Pareto-set obtained is compared with the CFD points (obtained while building the training data set). We can see that the Pareto-set is approaching the true Pareto-frontier of the simulated points in Fig. 7.5. It is insightful to see that $\eta_a/\eta_0 < 1$ can be achieved with a very small texture area. The extreme Pareto-point (corresponding to $\eta_a/\eta_0 > 1$) is not physically meaningful, but it is expected that the ASM-MOO algorithm will allow for its correction as the iterations proceed and the surrogate model accuracy is improved. Table 7.3 reports the Pareto-set values for both CFD data points and the ASM-MOO algorithm. This tradeoff information is valuable for designers who are interested in determining a texture design that best meets overall system design requirements.

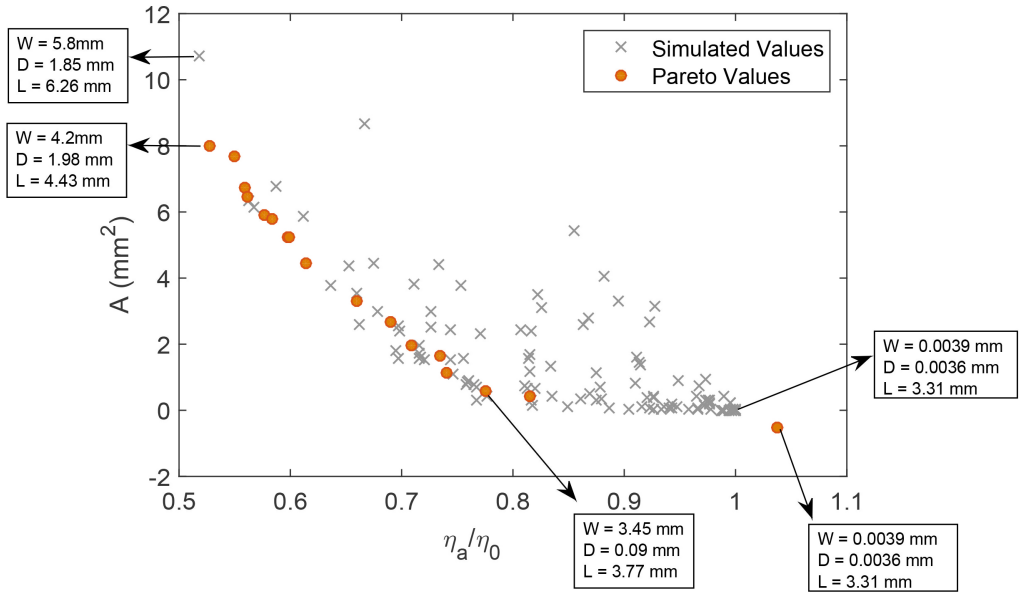

Figure 7.5: The CFD simulation outputs (gray markers) are shown along with the Pareto-set that is identified by the ASM-MOO algorithm (orange circles). By plotting all CFD simulation results we can qualitatively identify the location of the true Pareto set at the lower-left boundary of the attainable set. The Pareto-set shown here is the result of an initial set of six ASM-MOO iterations, and does not represent the converged optimal solution. Nonetheless, it is clear that the ASM-MOO algorithm is moving toward the true Pareto-set.

Table 7.3: The labeled set of Pareto-points (objective function values and corresponding optimal designs) at the end of six iterations (rows 2 and 3) of the ASM-MOO algorithm are compared with the Pareto-front from the CFD training data points (rows 1 and 4).

η_a/η_0	Area (mm^2)	W (mm)	D (mm)	L (mm)
0.518	10.719	5.797	1.849	6.260
0.527	8.000	4.202	1.978	4.432
0.775	0.578	3.453	0.090	3.772
1.00	1.4e-5	0.0039	0.0036	3.312

7.3 Conclusions and Future Work

Engineering design optimization problems are often characterized by multiple objectives and expensive simulations. As a strategy for reducing computational expense, surrogate modeling strategies have been developed and applied across a variety of engineering domains. In this article, one such strategy, Adaptive Surrogate Model coupled with Multi-Objective Optimization (ASM-MOO), was presented. A systematic formulation of the multi-objective problem and a detailed framework for the adaptive surrogate modeling was outlined. This algorithm also incorporated the use of design constraints in the sampling phase, which is an essential feature particularly in modeling systems that cannot be simulated in analytical example and is further extended to a fluid power component problem.

Future investigations will involve nonlinear sample constraints and design constraints evaluated using a SM. Alternative strategies for generating feasible samples should be explored (e.g., mapping a hypercube to F in the neighborhood of D_v). The case study provides great insights into plausible mictrotexture geometries for different design needs. However, it is limited currently to symmetric textures; ongoing work is addressing the case of asymmetric textures as well. Aside from texture geometry, we envision studying a larger optimization problem by including fluid properties such as viscosity, density etc., in the design space (i.e., simultaneous texture and fluid design). Other improvements include extension to 3D problems and non-Newtonian hydraulic fluids. The ASM-MOO method defined here is a local search algorithm; samples are taken from the neighborhood of the approximate Pareto set. As an extension, we would like to expand it to a global method by also sampling in regions of low information to improve global search properties. Another direction of work would involve investigating approximating functions beyond RBFs.

CHAPTER 8

Conclusion

The research presented in this thesis document was aimed at identifying efficient optimization algorithm catered toward material design problems in engineering. In the first part of the document, the motivation to use rheological materials to enhance design freedom was elaborated along with the challenges that exist pertaining to their use in engineering design. The subsequent part discussed the use of a specific class of rheologically complex materials, known as viscoelastic materials. The detailed modeling methodology and optimization strategies were presented with the help of a vibration isolator case study. The use of direct optimal control in realizing optimal target functions of viscoelastic materials was demonstrated and the results presented provide introductory insights into the broader problem.

The second section of the thesis dealt with surrogate-model based optimization. This technique was specifically applied to engineering design problems with multiple design objectives. A new algorithm was presented and detailed. The algorithm was then implemented using a simple analytical example and further extended to a fluid power problem and results were discussed.

The results presented in this thesis are meant to serve as introductory insights into using complex materials in engineering design. While they are not physically realizable at this stage, the author hopes that the work can motivate research aimed at design freedom and at the same time ensuring efficient design optimization.

APPENDIX A

High Frequency scaling of displacement amplitude

In Fig. 4.2, high-frequency power law scaling is indicated. This appendix provides derivations of these frequency-dependent scalings of the displacement amplitude, for multiple assumed constitutive models, used as reference slopes in Fig. 4.2.

A.1 Initial Case (Spring only)

With an input base displacement of

$$y(t) = Y_0 \sin(\omega t) \tag{A.1}$$

we consider assumed solution form

$$x(t) = X_0 \sin(\omega t + \phi) \tag{A.2}$$

For this scaling analysis, we consider the order $\mathcal{O}(\cdot)$ of front factors, dropping all trigonometric terms, as they are $\mathcal{O}(1)$. Inserting these assumptions into the equation of motion for the initial case (Eqn. (4.1) with $K(s) = 0$), we find the relation between force amplitude and acceleration amplitude

$$-k(X_0 - Y_0) \sim mX_0\omega^2 \tag{A.3}$$

This gives a nondimensional amplitude (normalized by the input magnitude) of

$$\frac{X_0}{Y_0} \sim \frac{1}{1 + \left(\frac{m}{k}\omega^2\right)} \tag{A.4}$$

Taking the limit of large frequency, where $\omega \gg \sqrt{\frac{k}{m}}$, or $\omega \gg \omega_n$

$$\lim_{\omega \gg \omega_n} \frac{X_0}{Y_0} \propto \frac{1}{\omega^2} \tag{A.5}$$

A.2 Spring + Linear Dashpot

Using identical assumptions and methods as in the initial case, the equation of motion for the mass m becomes

$$-k\left(X_0 - Y_0\right) - c\left(X_0\omega - Y_0\omega\right) \sim -mX_0\omega^2 \tag{A.6}$$

This gives a nondimensional amplitude of

$$\frac{X_0}{Y_0} \sim \frac{k + c\omega}{-m\omega^2 + c\omega + k} \tag{A.7}$$

Taking the limit of large frequency,

$$\lim_{\omega \to \infty} \frac{X_0}{Y_0} \propto \frac{1}{\omega} \tag{A.8}$$

A.3 Spring + Generalized Viscoelastic Element

As in Sec. 4.1.1, the equation of motion for mass m, attached to a base with a spring and generalized viscoelastic connection becomes:

$$-k(x-y) - \int_0^t K(s)\left[\dot{x}(t-s) - \dot{y}(t-s)\right] ds = m\ddot{x}(t) \tag{A.9}$$

The resulting motion is assumed to be of the expanded form:

$$x(t) = X_R \sin\omega t + X_i \cos\omega t \tag{A.10}$$

Thus the equation of motion has an assumed form of

$$-k(X_R \sin\omega t - X_i \cos\omega t) + kY \sin\omega t$$
$$-\int_0^t K(s)\left[\omega X_R\left(\cos\omega t\cos\omega s + \sin\omega t\sin\omega s\right) - \omega X_i\left(\sin\omega t\cos\omega s - \cos\omega t\sin\omega s\right)\right] ds$$

$$+ \int_0^t K(s)\omega Y \left(\cos\omega t \cos\omega + \sin\omega t \sin\omega s\right) ds$$
$$\sim -m\left[\omega^2 X_R \sin\omega t + \omega^2 X_i \cos\omega t\right] \quad \text{(A.11)}$$

A.3.1 Single mode Maxwell model

For a single mode Maxwell model, the viscoelastic parameterization is:

$$K(s) = K_m \exp -\frac{s}{\lambda} \quad \text{(A.12)}$$

Inserting this parameterization into the equation of motion and expanding gives:

$$\begin{aligned}
&- k\left[X_R \sin\omega t + X_i \cos\omega t\right] + kY \sin\omega t \\
&\quad - K_m\omega X_R \cos\omega t \int_0^t \exp\left(-\frac{s}{\lambda}\right)\cos\omega s ds \\
&\quad - K_m\omega X_R \sin\omega t \int_0^t \exp\left(-\frac{s}{\lambda}\right)\sin\omega s ds \\
&\quad + K_m\omega X_i \sin\omega t \int_0^t \exp\left(-\frac{s}{\lambda}\right)\cos\omega s ds \\
&\quad - K_m\omega X_i \cos\omega t \int_0^t \exp\left(-\frac{s}{\lambda}\right)\sin\omega s ds \\
&\quad + K_m\omega Y \cos\omega t \int_0^t \exp\left(-\frac{s}{\lambda}\right)\cos\omega s ds \\
&\quad + K_m\omega Y \sin\omega t \int_0^t \exp\left(-\frac{s}{\lambda}\right)\sin\omega s ds \\
&\qquad \sim -m\omega^2\left[X_R \sin\omega t + X_i \cos\omega t\right] \quad \text{(A.13)}
\end{aligned}$$

Evaluating each integral for the steady-state case ($t \to \infty$)

$$\begin{aligned}
&- k\left[X_R \sin\omega t + X_i \cos\omega t\right] + kY \sin\omega t \\
&\quad - K_m\omega X_R \cos\omega \frac{\left(\frac{1}{\lambda}\right)}{\left(\frac{1}{\lambda}\right)^2 + \omega^2} \\
&\quad - K_m\omega X_R \sin\omega \frac{\omega}{\left(\frac{1}{\lambda}\right)^2 + \omega^2}
\end{aligned}$$

$$
\begin{aligned}
&+ K_m\omega X_i \sin\omega \frac{\left(\frac{1}{\lambda}\right)}{\left(\frac{1}{\lambda}\right)^2+\omega^2} \\
&- K_m\omega X_i \cos\omega \frac{\omega}{\left(\frac{1}{\lambda}\right)^2+\omega^2} \\
&+ K_m\omega Y \cos\omega \frac{\left(\frac{1}{\lambda}\right)}{\left(\frac{1}{\lambda}\right)^2+\omega^2} \\
&- K_m\omega Y \sin\omega \frac{\omega}{\left(\frac{1}{\lambda}\right)^2+\omega^2} \\
&\sim -m\omega^2 \left[X_R \sin\omega t + X_i \cos\omega t\right] \quad \text{(A.14)}
\end{aligned}
$$

Grouping sine terms gives the relation

$$
X_R = \frac{1}{D}\left[-kY - K_m Y \frac{\omega^2}{\left(\frac{1}{\lambda}\right)^2+\omega^2} - K_m \frac{\frac{\omega}{\lambda}}{\left(\frac{1}{\lambda}\right)^2+\omega^2} X_i\right] \tag{A.15}
$$

Where

$$
D = m\omega^2 - k - K_m \frac{\omega^2}{\left(\frac{1}{\lambda}\right)^2+\omega^2} \tag{A.16}
$$

Similarly, grouping cosine terms of the equation of motion gives

$$
X_i = \frac{1}{\Delta}\left[-\frac{1}{D}K_m kY \frac{\frac{\omega}{\lambda}}{\left(\frac{1}{\lambda}\right)^2+\omega^2} - \frac{1}{D}K_m Y \frac{\frac{\omega^3}{\lambda}}{\left(\frac{1}{\lambda}\right)^2+\omega^2} - K_m Y \frac{\frac{\omega}{\lambda}}{\left(\frac{1}{\lambda}\right)^2+\omega^2}\right] \tag{A.17}
$$

Where

$$
\Delta = m\omega^2 - k + \frac{1}{D}K_m^2 \frac{\left(\frac{\omega}{\lambda}\right)^2}{\left(\frac{1}{\lambda}\right)^2+\omega^2} - K_m \frac{\omega^2}{\left(\frac{1}{\lambda}\right)^2+\omega^2} \tag{A.18}
$$

Now checking the limit of $\omega >> \frac{1}{\lambda}$ (i.e. $\omega \to \infty$)

$$
D \propto \omega^2 \tag{A.19}
$$

$$
\Delta \propto \omega^2 \tag{A.20}
$$

Thus plugging these in to the relations for X_R and X_i at the limit of $\omega \to \infty$ gives the high frequency behavior of:

$$
X_i \propto \frac{1}{\omega^3} \tag{A.21}
$$

$$
X_R \propto \frac{1}{\omega^2} \tag{A.22}
$$

The nondimensional amplitude is defined as

$$|X| = \left[X_R^2 + X_i^2\right]^{\frac{1}{2}} \tag{A.23}$$

And thus the full nondimensional amplitude high frequency behavior is:

$$|X| \propto \frac{1}{\omega^2} \tag{A.24}$$

A.3.2 Critical gel model

For the critical gel model, the viscoelastic parameterization is:

$$K(s) = S_k s^{-n} \tag{A.25}$$

Inserting this parameterization into the equation of motion and expanding gives:

$$\begin{aligned}
&-k\left[X_R \sin\omega t + X_i \cos\omega t\right] + kY \sin\omega t \\
&\qquad - S_k\omega X_R \cos\omega t \int_0^t s^{-n}\cos\omega s ds \\
&\qquad - S_k\omega X_R \sin\omega t \int_0^t s^{-n}\sin\omega s ds \\
&\qquad + S_k\omega X_i \sin\omega t \int_0^t s^{-n}\cos\omega s ds \\
&\qquad - S_k\omega X_i \cos\omega t \int_0^t s^{-n}\sin\omega s ds \\
&\qquad + S_k\omega Y \cos\omega t \int_0^t s^{-n}\cos\omega s ds \\
&\qquad + S_k\omega Y \sin\omega t \int_0^t s^{-n}\sin\omega s ds \\
&\qquad\qquad \sim -m\omega^2\left[X_R \sin\omega t + X_i \cos\omega t\right]
\end{aligned} \tag{A.26}$$

Evaluating each integral for the steady-state case ($t \to \infty$)

$$\begin{aligned}
&-k\left[X_R \sin\omega t + X_i \cos\omega t\right] + kY \sin\omega t \\
&\qquad - S_k\omega X_R \cos\omega t \left[\omega^{-1+n}\Gamma(1-n)\sin\left(\frac{n\pi}{2}\right)\right]
\end{aligned}$$

$$
\begin{aligned}
&- S_k\omega X_R \sin\omega t \left[\omega^{-1+n}\Gamma(1-n)\cos\left(\frac{n\pi}{2}\right)\right] \\
&+ S_k\omega X_i \sin\omega t \left[\omega^{-1+n}\Gamma(1-n)\sin\left(\frac{n\pi}{2}\right)\right] \\
&- S_k\omega X_i \cos\omega t \left[\omega^{-1+n}\Gamma(1-n)\sin\left(\frac{n\pi}{2}\right)\right] \\
&+ S_k\omega Y \cos\omega t \left[\omega^{-1+n}\Gamma(1-n)\cos\left(\frac{n\pi}{2}\right)\right] \\
&+ S_k\omega Y \sin\omega t \left[\omega^{-1+n}\Gamma(1-n)\sin\left(\frac{n\pi}{2}\right)\right] \\
&\sim -m\omega^2 \left[X_R \sin\omega t + X_i \cos\omega t\right] \quad \text{(A.27)}
\end{aligned}
$$

Grouping sine terms gives the relation

$$
X_R = \frac{1}{D}\left[kY - S_k Y\omega^n\Gamma(1-n)\sin\left(\frac{n\pi}{2}\right) - S_k X_i\omega^n\Gamma(1-n)\sin\left(\frac{n\pi}{2}\right)\right] \quad \text{(A.28)}
$$

Where:

$$
D = m\omega^2 - k - S_k\omega^n\Gamma(1-n)\cos\left(\frac{n\pi}{2}\right) \quad \text{(A.29)}
$$

Similarly, grouping cosine terms of the equation of motion gives

$$
\begin{aligned}
X_i = \frac{1}{\Delta}[-\frac{1}{D}S_k kY\omega^n\Gamma(1-n)\sin\left(\frac{n\pi}{2}\right) - \frac{1}{D}S_k^2 Y\omega^{2n}\left[\Gamma(1-n)\sin\left(\frac{n\pi}{2}\right)\right]^2 \quad \text{(A.30)} \\
-S_k Y\omega^n\Gamma(1-n)\cos\left(\frac{n\pi}{2}\right)]
\end{aligned}
$$

Where:

$$
\Delta = m\omega^2 - k + \frac{1}{D}S_k^2\left[\omega^n\Gamma(1-n)\sin\left(\frac{n\pi}{2}\right)\right]^2 - S_k\omega^n\Gamma(1-n)\sin\left(\frac{n\pi}{2}\right) \quad \text{(A.31)}
$$

Now checking the limit of $\omega >> \frac{1}{\lambda}$ (i.e. $\omega \to \infty$):

$$
D \propto \omega^2 \quad \text{(A.32)}
$$

$$
\Delta \propto \omega^2 \quad \text{(A.33)}
$$

Thus plugging these in to the relations for X_R and X_i at the limit of $\omega \to \infty$ gives the high frequency behavior of:

$$
X_i \propto \omega^{n-2} \quad \text{(A.34)}
$$

$$
X_R \propto \omega^{n-2} \quad \text{(A.35)}
$$

The nondimensional amplitude is defined as:

$$|X| = \left[X_R^2 + X_i^2\right]^{\frac{1}{2}} \tag{A.36}$$

And thus the full nondimensional amplitude high frequency behavior is

$$|X| \propto \omega^{n-2} \tag{A.37}$$

In summary, Eqs. (A.5),(A.8),(A.24),(A.37) are used as theoretical high-frequency limits of power-law slopes in Fig. 4.2.

REFERENCES

[1] E. Winsberg, "Computer Simulations in Science," in *The Stanford Encyclopedia of Philosophy*, Fall 2014 ed., E. N. Zalta, Ed., 2014.

[2] P. N. Koch, T. W. Simpson, J. K. Allen, and F. Mistree, "Statistical Approximations for Multidisciplinary Design Optimization: the Problem of Size," *Journal of Aircraft*, vol. 36, no. 1, pp. 275–286, 1999.

[3] J. Allison and D. Herber, "Multidisciplinary Design Optimization of Dynamic Engineering Systems," *AIAA Journal*, 2014.

[4] R. H. Ewoldt, "Extremely Soft: Design with Rheologically Complex Fluids," *Soft Robotics*, vol. 1, no. 1, pp. 12–20, 2014.

[5] P. Schümmer, "Mechanics of Non-Newtonian Fluids," *Chemie Ingenieur Technik*, vol. 51, no. 7, pp. 766–766, 1979. [Online]. Available: http://dx.doi.org/10.1002/cite.330510727

[6] R. Larson, *The Structure and Rheology of Complex Fluids*, ser. Topics in Chemical Engineering. OUP USA, 1999. [Online]. Available: http://books.google.com/books?id=Vt9fw_pf1LUC

[7] R. Shadwick, "Mechanical Design in Arteries," *Journal of Experimental Biology*, vol. 202, no. 23, pp. 3305–3313, 1999. [Online]. Available: http://jeb.biologists.org/content/202/23/3305.abstract

[8] M. Denny, "The Role of Gastropod Pedal Mucus in Locomotion," *Nature*, vol. 285, pp. 160–161, 1980.

[9] R. H. Ewoldt, A. E. Hosoi, and G. H. McKinley, "Nonlinear Viscoelastic Biomaterials: Meaningful Characterization and Engineering Inspiration," *Integrative and comparative biology*, vol. 49, no. 1, pp. 40–50, 2009.

[10] D. G. Jansson and S. M. Smith, "Design Fixation," *Design Studies*, vol. 12, no. 1, pp. 3 – 11, 1991. [Online]. Available: http://www.sciencedirect.com/science/article/pii/0142694X9190003F

[11] J. S. Linsey, I. Tseng, K. Fu, J. Cagan, K. L. Wood, and C. D. Schunn, "A Study of Design Fixation, its Mitigation and Perception in Engineering Design Faculty," *Journal of Mechanical Design*, vol. 132, no. 4, p. 041003, April 2010. [Online]. Available: http://d-scholarship.pitt.edu/22908/

[12] N. A. Bharadwaj, J. T. Allison, and R. H. Ewoldt, "Early-stage Design of Rheologically Complex Materials via Material Function Design Targets," *International Design Engineering Technical Conferences, Portland, OR, USA*, vol. 51, p. 61801, 2013.

[13] K. T. Ulrich, *Product Design and Development*. Tata McGraw-Hill Education, 2003.

[14] D. Roylance, "Engineering Viscoelasticity," 2001.

[15] H. Hu, Z. Yang, and H. Igarashi, "Aerodynamic Hysteresis of a Low-reynolds-number Airfoil," *Journal of Aircraft*, vol. 44, no. 6, pp. 2083–2086, 2007.

[16] G. A. Tompsett, L. Krogh, D. W. Griffin, and W. C. Conner, "Hysteresis and Scanning Behavior of Mesoporous Molecular Sieves," *Langmuir*, vol. 21, no. 18, pp. 8214–8225, 2005, pMID: 16114924. [Online]. Available: http://dx.doi.org/10.1021/la050068y

[17] R. B. Bird, R. Armstrong, and O. Hassger, *Dynamics of Polymeric Liquids: Volume 1 Fluid Mechanics*, 2nd ed. New York: John Wiley and Sons, Inc., 1987.

[18] J. D. Ferry, *Viscoelastic Properties of Polymers*, 3rd ed. Wiley, 1980.

[19] J. M. Dealy, "Official Nomenclature for Material Functions Describing the Response of a Viscoelastic Fluid to Various Shearing and Extensional Deformations," *Journal of Rheology*, vol. 39, no. 1, pp. 253–265, 1995.

[20] S. Breuer and E. T. Onat, "On Uniqueness in Linear Elasticity," *Quarterly of Applied Mathematics*, vol. 19, no. 4, pp. 355–359, 1962.

[21] I. N. Rabotnov, *Elements of Hereditary Solid Mechanics*. Moscow: Mir, 1977.

[22] F. Chambon and H. H. Winter, "Linear Viscoelasticity at the Gel Point of a Cross-linking PDMS with Imbalanced Stoichiometry," *Journal of Rheology*, vol. 31, no. 8, pp. 683–697, 1987.

[23] H. H. Winter and F. Chambon, "Analysis of Linear Viscoelasticity of a Cross-linking Polymer at the Gel Point," *Journal of Rheology*, vol. 30, no. 2, pp. 367–382, 1986.

[24] H. H. Winter and M. Mours, "Rheology of Polymers Near Liquid-Solid Transitions," in *Neutron Spin Echo Spectroscopy, Viscoelasticity, Rheology (Advances in Polymer Science)*, vol. 134 ed. Heidelberg: Springer Berlin, 1997, pp. 165–234.

[25] F. Cordobes, P. Partal, and A. Guerrero, "Rheology and Microstructure of Heat-induced Egg Yolk Gels," *Rheologica Acta*, vol. 43, no. 2, pp. 184–195, Mar. 2004. [Online]. Available: http://link.springer.com/10.1007/s00397-003-0338-3

[26] P. Kollmannsberger and B. Fabry, "Linear and Nonlinear Rheology of Living Cells," *Annual Review of Materials Research*, vol. 41, no. 1, pp. 75–97, 2011.

[27] R. Corman, L. Rao, J. Allison, and R. Ewoldt, "Design with Rheologically Complex Materials via Material Function Design Targets," *In review, Journal of Mechanical Design*, 2015.

[28] M. Athans and P. L. Falb, *Optimal Control: an Introduction to the Theory and Its Applications*. Dover Publications, McGraw-Hill, 2006.

[29] J. T. Betts, *Practical Methods for Optimal Control and Estimation Using Nonlinear Programming*. SIAM, 2010.

[30] J. T. Allison, T. Guo, and Z. Han, "Co-Design of an Active Suspension Using Simultaneous Dynamic Optimization," *Journal of Mechanical Design*, vol. 136, no. 8, p. 081003, 2014.

[31] C. D. Johnson, "Design of Passive Damping Systems," *Journal of Mechanical Design*, vol. 117, no. B, p. 171, 1995.

[32] H. H. Hilton, "Optimum Linear and Nonlinear Viscoelastic Designer Functionally Graded Materials - Characterizations and Analysis," *Composites Part A: Applied Science and Manufacturing*, vol. 36, no. 10, pp. 1329–1334, 2005.

[33] H. H. Hilton, D. H. Lee, and A. R. A. El Fouly, "Generalized Viscoelastic Designer Functionally Graded Auxetic Materials Engineered/tailored for Specific Task Performances," *Mechanics of Time-Dependent Materials*, vol. 12, no. 2, pp. 151–178, 2008.

[34] M. Rahman, *Integral Equations and Their Applications* , 1st ed. WIT Press, 2007.

[35] A.-M. Wazwaz, *Linear and Nonlinear Integral Equations: Methods and Applications*, 1st ed. Springer Publishing Company, Incorporated, 2011.

[36] C. Baker, *The Numerical Treatment of Integral Equations*, ser. Monographs on Numerical Analysis Series. Oxford: Clarendon Press, 1977. [Online]. Available: http://books.google.com/books?id=B9sIAQAAIAAJ

[37] Q. Wang, K. Wang, and S. Chen, "Least Squares Approximation Method for the Solution of Volterra Fredholm Integral Equations," *Journal of Computational and Applied Mathematics*, vol. 272, pp. 141 – 147, 2014. [Online]. Available: http://www.sciencedirect.com/science/article/pii/S0377042714002465

[38] H. Brunner, "A Survey of Recent Advances in the Numerical Treatment of Volterra Integral and Integro-differential Equations," *Journal of Computational and Applied Mathematics*, vol. 8, no. 3, pp. 213 – 229, 1982. [Online]. Available: http://www.sciencedirect.com/science/article/pii/0771050X82900444

[39] H. Brunner, "Implicit Runge-Kutta-Nystrm Methods for General Second-order Volterra Integro-differential Equations," *Computers & Mathematics with Applications*, vol. 14, no. 7, pp. 549 – 559, 1987. [Online]. Available: http://www.sciencedirect.com/science/article/pii/0898122187900502

[40] H. Brunner and N. Yan, "Finite Element Methods for Optimal Control Problems Governed by Integral Equations and Integro-differential Equations," *Numerische Mathematik*, vol. 101, no. 1, pp. 1–27, 2005. [Online]. Available: http://dx.doi.org/10.1007/s00211-005-0608-3

[41] C. T. Baker, "A Perspective on the Numerical Treatment of Volterra Equations." *Journal of Computational and Applied Mathematics*, vol. 125, no. 12, pp. 217 – 249, 2000, numerical Analysis 2000. Vol. VI: Ordinary Differential Equations and Integral Equations. [Online]. Available: http://www.sciencedirect.com/science/article/pii/S0377042700004702

[42] J. A. Dixon, "Generalized Reducible Quadrature Methods for Volterra Integral and Integro-differential Equations," *Journal of Computational and Applied Mathematics*, vol. 16, no. 1, pp. 27 – 42, 1986. [Online]. Available: http://www.sciencedirect.com/science/article/pii/0377042786901718

[43] M. H. Celik, I. Muslu, and B. Bayraktar, "A Numerical Approach to Solve Integro-Differential Equations System," *European Journal of Scientific Research*, vol. 80, no. 4, pp. 552–559, 2012.

[44] G. Adomian, "A Review of the Decomposition Method and Some Recent Results for Nonlinear Equations," *Computers & Mathematics with Applications*, vol. 21, no. 5, pp. 101 – 127, 1991. [Online]. Available: http://www.sciencedirect.com/science/article/pii/089812219190220X

[45] G. Adomian, "Integral Equations," in *Solving Frontier Problems of Physics: The Decomposition Method*, ser. Fundamental Theories of Physics. Springer Netherlands, 1994, vol. 60, pp. 224–227. [Online]. Available: http://dx.doi.org/10.1007/978-94-015-8289-6_10

[46] M. Hosseini, "Adomian Decomposition Method with Chebyshev Polynomials," *Applied Mathematics and Computation*, vol. 175, no. 2, pp. 1685 – 1693, 2006. [Online]. Available: http://www.sciencedirect.com/science/article/pii/S0096300305007241

[47] M. Hosseini and H. Nasabzadeh, "On the Convergence of Adomian Decomposition Method," *Applied Mathematics and Computation*, vol. 182, no. 1, pp. 536 – 543, 2006. [Online]. Available: http://www.sciencedirect.com/science/article/pii/S0096300306003614

[48] B. Batiha, M. Noorani, and I. Hashim, "Numerical Solutions of the Nonlinear Integro-differential Equations," *Int. J. Open Problems Compt. Math*, vol. 1, no. 1, pp. 34–42, 2008.

[49] Z. Jiang, S. J. Kim, S. Plude, and R. Christenson, "Real-time Hybrid Simulation of a Complex Bridge Model with MR Dampers Using the Convolution Integral Method," *Smart Materials and Structures*, vol. 22, no. 10, p. 105008, 2013. [Online]. Available: http://stacks.iop.org/0964-1726/22/i=10/a=105008

[50] J. T. Edwards, N. J. Ford, and J. A. Roberts, "The Numerical Simulation of the Qualitative Behaviour of Volterra Integro-Diffeential Equations," Ph.D. dissertation, Chester College, UK, 2001.

[51] C. Lubich, "Convolution Quadrature and Discretized Operational Calculus. ii," *Numerische Mathematik*, vol. 52, no. 4, pp. 413–425, 1988. [Online]. Available: http://dx.doi.org/10.1007/BF01462237

[52] E. Cuesta, C. Lubich, and C. Palencia, "A Survey of Recent Advances in the Numerical Treatment of Volterra Integral and Integro-differential Equations," Math. Comp, Tech. Rep., 2006.

[53] C. Zhang and S. Vandewalle, "General Linear Methods for Volterra Integro-differential Equations with Memory," *SIAM J. Sci. Comput.*, vol. 27, no. 6, pp. 2010–2031, Dec. 2005. [Online]. Available: http://dx.doi.org/10.1137/040607058

[54] M. Peszynska, "Analysis of an Integro-differential Equation Arising from Modelling of Flows with Fading Memory Through Fissured Media," *Partial Diff. Eqs*, vol. 8, pp. 159–173, 1995.

[55] M. Peszynska, "Finite Element Approximation of Diffusion Equations with Convolution Terms ," *Mathematics of Computation of the American Mathematical Society*, vol. 65, no. 215, pp. 1019–1037, 1996.

[56] D. R. Herber and J. T. Allison, "Wave Energy Extraction Maximization in Irregular Ocean Waves using Pseudospectral Methods," in *International Design Engineering Technical Conferences, Portland, OR, USA, No. DETC2013-12600*. ASME, 2013, p. V03AT03A018.

[57] Z. Yu and J. Falnes, "State-space Modelling of a Vertical Cylinder in Heave," *Applied Ocean Research*, vol. 17, no. 5, pp. 265 – 275, 1995. [Online]. Available: http://www.sciencedirect.com/science/article/pii/0141118796000028

[58] H. Sussmann and J. Willems, "300 Years of Optimal Control: from the Brachystochrone to the Maximum Principle ," *Control Systems, IEEE*, vol. 17, no. 3, pp. 32–44, Jun 1997.

[59] D. R. Herber, "Dynamic System Design Optimization of Wave Energy Converters Utilizing Direct Transcription," M.S. thesis, Univ. of Illinois at Urbana-Champaign, 2014.

[60] L. T. Biegler, *Nonlinear Programming: Concepts, Algorithms, and Applications to Chemical Processes*. SIAM, 2010.

[61] U. Ascher and L. Petzold, *Computer Methods for Ordinary Differential Equations and Differential-Algebraic Equations*. Society for Industrial and Applied Mathematics, 1998. [Online]. Available: http://books.google.com/books?id=AqQ6QMthXkMC

[62] D. R. Herber, "Solving Optimal Control Problems using Simscape Models for State Derivatives," Engineering System Design Lab, Urbana, IL, USA, Technical Report UIUC-ESDL-2014-01, July 2014. [Online]. Available: http://hdl.handle.net/2142/50015

[63] D. J. Inman, *Engineering Vibration*, 4th ed. Prentice-Hall, Inc., 2001.

[64] G. G. Wang and S. Shan, "Review of Metamodeling Techniques in Support of Engineering Design Optimization," *Journal of Mechanical Design*, vol. 129, no. 4, pp. 370–380, 2007. [Online]. Available: http://dx.doi.org/10.1115/1.2429697

[65] N. V. Queipo, R. T. Haftka, W. Shyy, T. Goel, R. Vaidyanathan, and P. K. Tucker, "Surrogate-based Analysis and Optimization," *Progress in Aerospace Sciences*, vol. 41, no. 1, pp. 1 – 28, 2005. [Online]. Available: http://www.sciencedirect.com/science/article/pii/S0376042105000102

[66] G. Liu, X. Han, and C. Jiang, "A Novel Multi-objective Optimization Method Based on an Approximation Model Management Technique," *Computer Methods in Applied Mechanics and Engineering*, vol. 197, no. 33?40, pp. 2719 – 2731, 2008. [Online]. Available: http://www.sciencedirect.com/science/article/pii/S0045782508000029

[67] G. Chen, X. Han, G. Liu, C. Jiang, and Z. Zhao, "An Efficient Multi-objective Optimization Method for Black-box Functions Using Sequential Approximate Technique," *Appl. Soft Comput.*, vol. 12, no. 1, pp. 14–27, Jan. 2012.

[68] J. Barthelemy and R. Haftka, "Approximation Concepts for Optimum Structural Design - a Review," *Structural Optimization*, vol. 5, no. 3, pp. 129–144, 1993. [Online]. Available: http://dx.doi.org/10.1007/BF01743349

[69] J. Zhou and L.-S. Turng, "Adaptive Multiobjective Optimization of Process Conditions for Injection Molding Using a Gaussian Process Approach," *Advances in Polymer Technology*, vol. 26, no. 2, pp. 71–85, 2007.

[70] A. Booker, J. Dennis, J.E., P. Frank, D. Serafini, V. Torczon, and M. Trosset, "A Rigorous Framework for Optimization of Expensive Functions by Surrogates," *Structural optimization*, vol. 17, no. 1, pp. 1–13, 1999. [Online]. Available: http://dx.doi.org/10.1007/BF01197708

[71] C. Wang, Q. Duan, W. Gong, A. Ye, Z. Di, and C. Miao, "An Evaluation of Adaptive Surrogate Modeling Based Optimization with Two Benchmark Problems ," *Environmental Modelling Software*, vol. 60, no. 0, pp. 167 – 179, 2014.

[72] B. Wilson, D. Cappelleri, T. Simpson, and M. Frecker, "Efficient Pareto Frontier Exploration using Surrogate Approximations," *Optimization and Engineering*, vol. 2, no. 1, pp. 31–50, 2001. [Online]. Available: http://dx.doi.org/10.1023/A%3A1011818803494

[73] Y. Li, G. Fadel, and M. Wiecek, "Approximating Pareto Curves Using the Hyper-Ellipse," *American Institute of Aeronautics and Astronautics*, 1998.

[74] S. Shan and G. G. Wang, "An Efficient Pareto Set Identification Approach for Multiobjective Optimization on Black-Box Functions," *Journal of Mechanical Design*, 2004.

[75] M. J. Alexander, J. T. Allison, P. Y. Papalambros, and D. J. Gorsich, "Constraint Management of Reduced Representation Variables in Decomposition-based Design Optimization," *Journal of Mechanical Design*, vol. 133, no. 10, p. 101014, 2011.

[76] S. Kitayama, M. Arakawa, and K. Yamazaki, "Sequential Approximate Optimization Using Radial Basis Function Network for Engineering Optimization," *Optimization and Engineering*, vol. 12, no. 4, pp. 535–557, 2011. [Online]. Available: http://dx.doi.org/10.1007/s11081-010-9118-y

[77] L. Gururaja Rao, J. Schuh, R. H. Ewoldt, and J. T. Allison, "On Using Adaptive Surrogate Modeling in Design For Efficient Fluid Power," in *To appear in ASME 2015 International Design Engineering Technical Conferences*, no. DETC2015-46832, Boston, MA, USA, Aug. 2015.

[78] S. Ferreira, R. Bruns, H. Ferreira, G. Matos, J. David, G. Brando, E. da Silva, L. Portugal, P. dos Reis, A. Souza, and W. dos Santos, "Box-behnken Design: an Alternative for the Optimization of Analytical Methods," *Analytica Chimica Acta*, vol. 597, no. 2, pp. 179 – 186, 2007. [Online]. Available: http://www.sciencedirect.com/science/article/pii/S0003267007011671

[79] T. W. Simpson, J. K. Allen, J. S. Colton, R. G. Heikes, W. Rosen, and D. P. Schrage, "A Concept Exploration Method for Product Family Design," in Mechanical Engineering. Atlanta, GA: Georgia Institute of Technology, Tech. Rep., 1998.

[80] J.-S. Park, "Optimal Latin-hypercube Designs for Computer Experiments ," *Journal of Statistical Planning and Inference*, vol. 39, no. 1, pp. 95 – 111, 1994. [Online]. Available: http://www.sciencedirect.com/science/article/pii/0378375894901155

[81] J. Sacks, W. J. Welch, T. J. Mitchell, and H. P. Wynn, "Design and Analysis of Computer Experiments," *Statistical Science*, vol. 4, no. 4, pp. 409–423, 1989. [Online]. Available: http://dx.doi.org/10.2307/2245858

[82] G. G. Wang, "Adaptive Response Surface Method Using Inherited Latin Hypercube Design Points," *Journal of Mechanical Design*, June 2003. [Online]. Available: http://www.umanitoba.ca/faculties/engineering/mech_and_ind/prof/wang/index_files/Jmd-arsm.PDF

[83] B. Tang, "Orthogonal Array-Based Latin Hypercubes," *Journal of the American Statistical Association*, vol. 88, no. 424, pp. 1392–1397, 1993. [Online]. Available: http://www.tandfonline.com/doi/abs/10.1080/01621459.1993.10476423

[84] N. Cressie, "Spatial Prediction and Ordinary Kriging," *Mathematical Geology*, vol. 20, no. 4, pp. 405–421, 1988. [Online]. Available: http://dx.doi.org/10.1007/BF00892986

[85] J. Suykens, J. Vandewalle, and B. de Moor, *Artificial Neural Networks for Modelling and Control of Non-Linear Systems*. Springer, 1996. [Online]. Available: https://books.google.com/books?id=cV7nkW9gMMgC

[86] N. Dyn, D. Levin, and S. Rippa, "Numerical Procedures for Surface Fitting of Scattered Data by Radial Functions," *SIAM Journal on Scientific and Statistical Computing*, vol. 7, no. 2, pp. 639–659, 1986. [Online]. Available: http://dx.doi.org/10.1137/0907043

[87] H. Fang and M. F. Horstemeyer, "Global Response Approximation with Radial Basis Functions," *Engineering Optimization*, vol. 38, no. 4, pp. 407–424, 2006. [Online]. Available: http://dx.doi.org/10.1080/03052150500422294

[88] J. H. Friedman, "Multivariate Adaptive Regression Splines," *Ann. Statist*, 1991.

[89] C. de Boor and A. Ron, "On Multivariate Polynomial Interpolation," *Constructive Approximation*, vol. 6, no. 3, pp. 287–302, 1990. [Online]. Available: http://dx.doi.org/10.1007/BF01890412

[90] P. Langley and H. A. Simon, "Applications of Machine Learning and Rule Induction," *Commun. ACM*, vol. 38, no. 11, pp. 54–64, Nov. 1995. [Online]. Available: http://doi.acm.org/10.1145/219717.219768

[91] R. Jin, W. Chen, and T. Simpson, "Comparative Studies of Metamodelling Techniques under Multiple Modelling Criteria," *Structural and Multidisciplinary Optimization*, vol. 23, no. 1, pp. 1–13, 2001. [Online]. Available: http://dx.doi.org/10.1007/s00158-001-0160-4

[92] N. Stander, W. Roux, M. Giger, M. Redhe, N. Fedorova, and J. Haarhoff, "A Comparison of Meta-modeling Techniques for Crashworthiness Optimization ," *10th AIAA/ISSMO Multidisciplinary Analysis and Optimization Conference*, pp. AIAA–2004–4489, 2004.

[93] T. Goel, R. Haftka, W. Shyy, and N. Queipo, "Ensemble of Surrogates," *Structural and Multidisciplinary Optimization*, vol. 33, no. 3, pp. 199–216, 2007. [Online]. Available: http://dx.doi.org/10.1007/s00158-006-0051-9

[94] A. P. Deshmukh and J. T. Allison, "Design of Nonlinear Dynamic Systems Using Surrogate Models of Derivative Functions," *Proceedings of IDETC/CIE 2013*, vol. 51, p. 61801, 2013.

[95] H. Fang, M. Rais-Rohani, Z. Liu, and M. F. Horstemeyer, "A Comparative Study of Metamodeling Methods for Multiobjective Crashworthiness Optimization," *Comput. Struct.*, vol. 83, no. 25-26, pp. 2121–2136, Sep. 2005. [Online]. Available: http://dx.doi.org/10.1016/j.compstruc.2005.02.025

[96] A. Forrester, A. Sobester, and A. Keane, *Engineering Design via Surrogate Modelling: a Practical Guide*. John Wiley & Sons, 2008.

[97] L. Zadeh, "Optimality and Non-scalar-valued Performance Criteria," *IEEE Transactions on Automatic Control*, vol. 8, no. 1, pp. 59–60, Jan 1963.

[98] P. Farquhar, "Advances in Multiattribute Utility Theory," *Theory and Decision*, vol. 12, no. 4, pp. 381–394, 1980. [Online]. Available: http://dx.doi.org/10.1007/BF00131317

[99] D. Kalyanmoy, *Multi-Objective Optimization Using Evolutionary Algorithms*. New York, NY, USA: John Wiley & Sons, Inc., 2001.

[100] K. Deb, A. Pratap, S. Agarwal, and T. Meyarivan, "A Fast and Elitist Multiobjective Genetic Algorithm: NSGA-II," *Trans. Evol. Comp*, vol. 6, no. 2, pp. 182–197, Apr. 2002. [Online]. Available: http://dx.doi.org/10.1109/4235.996017

[101] C. M. Fonseca and P. J. Fleming, "Genetic Algorithms for Multiobjective Optimization: Formulation, Discussion and Generalization," in *Proceedings of the 5th International Conference on Genetic Algorithms*. San Francisco, CA, USA: Morgan Kaufmann Publishers Inc., 1993. [Online]. Available: http://dl.acm.org/citation.cfm?id=645513.657757 pp. 416–423.

[102] J. D. Foley, A. van Dam, S. K. Feiner, and J. F. Hughes, *Computer Graphics: Principles and Practice*. Boston, MA, USA: Addison-Wesley Longman Publishing Co., Inc., 1990.

[103] R. J. Malak and C. J. Paredis, "Using Support Vector Machines to Formalize the Valid Input Domain of Predictive Models in Systems Design Problems," *Journal of Mechanical Design*, vol. 132, no. 10, p. 101001, 2010.

[104] M. Meckesheimer, A. J. Booker, R. R. Barton, and T. W. Simpson, "Computationally Inexpensive Metamodel Assessment Strategies," *AIAA Journal*, vol. 40, pp. 2053–2060, 2002.

[105] M. Meckesheimer, "A Framework For Metamodel-Based Design: Subsystem Metamodel Assessment and Implementation Issues," Ph.D. dissertation, The Pennsylvania State University, University Park, PA, 2001.

[106] D. Gorissen, I. Couckuyt, P. Demeester, T. Dhaene, and K. Crombecq, "A surrogate modeling and adaptive sampling toolbox for computer based design," *J. Mach. Learn. Res.*, vol. 11, pp. 2051–2055, Aug. 2010. [Online]. Available: http://dl.acm.org/citation.cfm?id=1756006.1859919

[107] D. Meagher, *Octree Encoding: a New Technique for the Representation, Manipulation and Display of Arbitrary 3-D Objects by Computer*. Electrical and Systems Engineering Department Rensseiaer Polytechnic Institute Image Processing Laboratory, 1980. [Online]. Available: http://books.google.com/books?id=CgRPOAAACAAJ

[108] D. Bertsekas, *Nonlinear Programming*. Athena Scientific, 1995. [Online]. Available: http://books.google.com/books?id=QeweAQAAIAAJ

[109] M. T. Johnston, W. P. King, and R. H. Ewoldt, "Shear Stress Characteristics of Microtextured Surfaces in Gap-controlled Hydrodynamic Lubrication," *Tribology International*, vol. 82, Part A, no. 0, pp. 123 – 132, 2015.

[110] J. Schuh and R. H. Ewoldt, "Effects of Surface Texture Depth Profile on Decreasing Friction in Hydrodynamic Lubricated Sliding Friction," *In preparation*.